



מכון ויצמן למדע

WEIZMANN INSTITUTE OF SCIENCE

Thesis for the degree  
**Master of Science**

Submitted to the Scientific Council of the  
Weizmann Institute of Science  
Rehovot, Israel

עבודת גמר (תזה) לתואר  
**מוסמך למדעים**

מוגשת למועצה המדעית של  
מכון ויצמן למדע  
רחובות, ישראל

by  
**David Columbus**

מאת  
**דויד קולומבוס**

**חקירת תהליכים דינמיים על פני שטח בבטריות ליתיום  
באמצעות כלים חישוביים וניסיוניים**

**Examination of Interfacial Lithium Ion  
Transport through Computational and  
Experimental Techniques**

Advisor:  
**Dr. Michal Leskes**

מנחה:  
**ד"ר מיכל לסקס**

January 2022

טבת תשפ"ב

## Table of Contents

.....	1
.....	1
.....	1
.....	1
.....	1
<b>1. Abstract.....</b>	<b>3</b>
<b>2. List of abbreviations .....</b>	<b>4</b>
<b>3. Introduction.....</b>	<b>4</b>
<b>4. Objectives.....</b>	<b>6</b>
4.1 Investigate SEI properties by CEST.....	6
4.2 Modeling interfacial Li exchange process at OCV.....	6
4.3 Thesis structure (a general comment for the reader).....	7
<b>5. CEST .....</b>	<b>7</b>
5.1 Motivation and approach.....	7
5.2 Experimental .....	8
5.2.1 Materials .....	8
5.2.2 Li dendrites formation .....	8
5.2.3 NMR .....	8
5.3 Theory .....	8
5.4 Results .....	10
5.4.1 Quantification of exchange rate using varying saturation power (QUESP) .....	11
5.4.2 Z-spectra .....	12
5.4.3 $\text{Limetal0} \rightleftharpoons \text{Lielelectrolyte} + \text{or } \text{Limetal0} \rightleftharpoons \text{LiSEI} + ?$ .....	13
5.4.4 Fitting .....	15
5.5 Conclusions & outlook .....	15
<b>6. Li isotope exchange .....</b>	<b>15</b>
6.1. Motivation and approach.....	15
6.2. Three time-dependent processes .....	16
6.2.1. Li ion exchange .....	16
6.2.2. Corrosion (native SEI formation) .....	17
6.2.3. Self-diffusion of Li metal atoms .....	17
6.3. Experimental .....	17
6.3.1. Sample preparation .....	17
6.3.2. NMR.....	17
6.3.3. Self-diffusion experiment .....	18
6.3.4. Coated samples .....	18
6.4. Model .....	18
6.4.1. Motivation .....	18
6.4.2. Agent-based modeling using NetLogo .....	18
6.4.3. The model.....	19

<b>6.5. Results .....</b>	<b>24</b>
6.5.1. Experimental.....	24
6.5.2. Simulation fitting .....	25
6.5.3. Generalization of the model.....	26
6.5.4. Coated samples – collaboration with MIT .....	26
<b>6.6. Conclusions &amp; outlook .....</b>	<b>28</b>
<b>7. Appendixes.....</b>	<b>28</b>
<b>7.1. CEST.....</b>	<b>28</b>
7.1.1. Li dendrites formation .....	28
7.1.2. Estimating the surface area of Li dendrites .....	29
7.1.3. Estimating the fraction of Li atoms on the surface of Li dendrites.....	30
7.1.4. QUESP of Li dendrites + Li metal bulk.....	31
<b>7.2. Isotope exchange .....</b>	<b>31</b>
7.2.1. NetLogo's <i>diffuse</i> function.....	31
7.2.2. Stability of the fitting parameters .....	33
7.2.3. Isotope exchange - Gunnarsdóttir et al. ....	33
7.2.4. Sensitivity analysis to the skin effect .....	34
7.2.5. Sensitivity to surface area.....	36
7.2.6. Fitted $j_{ex}(t)$ .....	36
<b>8. References.....</b>	<b>36</b>
<b>9. Acknowledgments .....</b>	<b>39</b>

## 1. Abstract

Li metal batteries (LMB) are, theoretically, the best candidates to replace Li-ion batteries (LIB) and spearhead the revolution towards a more sustainable and carbon-free (electric) vehicle industry. However, finding a metal-based system that has satisfying performance, let alone developing a scaled-up device that stands in the market criteria, is not yet achievable. In part, this failure stems from the lack of understanding of the complex, multiresolution, dynamic nature of LMB – despite the great (and increased) efforts invested in its research. Special interest is given to the solid electrolyte interphase (SEI), a passivation layer formed on the Li metal anode which has been titled “the most important but least understood component in the battery.” *Most important* – since it has been proven to affect the battery performance dramatically, and *least understood* – since there are almost no tools to characterize this ultra-thin solid layer at the molecular level. Therefore, to fill these gaps, we believe that efforts should be focused on developing new characterization methodologies. Nuclear magnetic resonance (NMR) is an excellent tool for LMB research allowing high-sensitivity and high-resolution quantification while being non-invasive and non-destructive.

In this thesis, we present new experimental & computational tools to probe and quantify Li transport across metal||SEI||electrolyte systems, including metal $\rightleftharpoons$ SEI exchange, which is a process that is almost completely overlooked in research literature. We used  $^6\text{-}^7\text{Li}$  isotopic labeling to monitor

metal $\rightleftharpoons$ electrolyte Li exchange in different electrolytes, subsequently developing a numerical model quantifying this complex time-dependent process. The results showed significance variance between electrolytes, indicating on different transport properties. In an additional project, we used chemical exchange saturation transfer (CEST) NMR to probe metal $\rightleftharpoons$ SEI solid-solid interaction, demonstrating the first implementation of this methodology to probe exchange between two solids. Using this method, we have been able to characterize physical properties of SEI formed in different systems.

Collectively, we believe the work carried out in this thesis forms the basis for implementing methodologies to guide coherent and systematic LMB designs.

## 2. List of abbreviations

CEST	Chemical exchange saturation transfer
DMC	Dimethyl carbonate
DME	Dimethyl ether
DOL	1,3-Dioxolane
EC	Ethylene carbonate
FEC	Fluoroethylene carbonate
EIS	Electrochemical impedance spectroscopy
LIB	Lithium ion batteries
LiTFSI	Lithium bis(trifluoromethanesulfonyl)imide
LMB	Lithium metal batteries
MSE	Mean squared error
OCV	Open-circuit voltage
SA	Surface area
SEI	Solid electrolyte interphase
SEM	Scanning Electron Microscopy
SHE	Standard hydrogen electrode
ssNMR	Solid-state nuclear magnetic resonance
XPS	X-Ray Photoelectron Spectroscopy

## 3. Introduction

The demand for rechargeable batteries that meet the requirements of both performance and sustainability is exponentially increasing, as well as the search for technologies that will actualize this unmet need. A future battery for electric vehicles, for example, should have a long lifetime, fast charging, high power and energy densities, and obviously, be safe to use<sup>1</sup>. On the other hand, the materials abundance, accessibility, recyclability, and other environmental aspects should also be considered. Among the potential candidates for anode materials, Li metal is most appealing due to its high theoretical specific capacity (3860 mAh/g) and low negative redox potential (-3.04V vs. SHE), both result in ultra-high energy density.

Despite having these extraordinary properties, Li metal anodes are problematic due to their tendency for poor cycling behavior, caused by the extreme reactivity of Li metal. The charging process is characterized by an uneven Li deposition and mossy/dendritic interface<sup>2,3,4</sup>. In general, two main

drawbacks keep rechargeable Li-metal batteries impractical: (i) cell inefficiency, which is reflected in constant electrolyte consumption, poor cycle life, loss of active material (“dead lithium”)<sup>5,6</sup>, and (ii) safety hazards such as short-circuits, caused by the combination of the uncontrolled dendrites growth in the presence of flammable organic solvents in the electrolyte.

Once the Li metal anode comes in contact with the liquid, electrolyte species decompose on the anode surface to form SEI<sup>7,8,9</sup>. The resulting material covering the whole of the anode surface is a thin layer with a thickness of 10-100 nm, made of organic and inorganic phases (*Figure 1*). It is hard to overestimate the importance of the SEI and its ability to affect the cell's performance: the “strategic” location (i.e., at the anode – electrolyte interface) makes each of its chemical and physical properties (composition, density, uniformity, stability, interaction with the neighboring phases) a crucial factor in determining the Li transport and deposition behavior<sup>10</sup>. Therefore, a good SEI or a bad one could be the difference between a successful battery cell or a failure. A beneficial SEI should be chemically stable, electrically insulating (i.e., blocks electrons flow), yet ion-

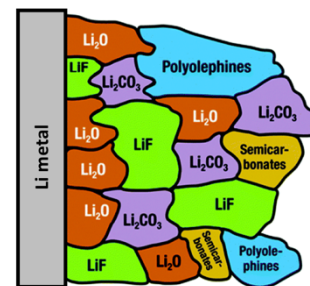


*Figure 1: An illustration of the mosaic model of the SEI formed on Li metal in carbonate-based electrolytes.*

conducting (allows efficient ions mobility through it). It is important to distinguish between two types of SEIs: the one formed spontaneously at open-circuit voltage (OCV), referred to as native SEI, and the one formed under electrochemical conditions, i.e., during battery cycling (referred to as galvanic SEI). Whether the native SEI and the galvanic SEI are similar in chemical composition and functionality is not fully understood.

Understanding the crucial role of SEI in batteries makes it the subject of extensive research, and continuous efforts are made to find and optimize the ideal electrolyte composition that leads to a desirable SEI. Therefore, methodologies and tools that could be used to characterize and analyze the SEI are highly needed. However, a significant issue that inhibits the development in the field is the inability to probe the SEI and the dynamic processes occurring at the interface *directly*. The challenge arises due to various reasons: (i) the SEI is composed of many different chemical phases, (ii) the SEI is minor compare to the anode/electrolyte populations (in terms of the total number of moles), and (iii) the system cannot be exposed to air or to high energy (due to Li metal extreme sensitivity and the volatile nature of some of the SEI components), which limits the available characterization methods even more. Consequently, the current tools cannot obtain accurate and unequivocal conclusions about the microscopic nature of the processes in a battery cell. Electrochemical Impedance Spectroscopy (EIS) is being used, for example, to determine the resistivity of the different types of SEI layers<sup>11,12,13</sup>. However, it relies on indirect interpretation, so it lacks the essential information regarding the SEI's specific chemical and physical properties. Other methods, such as X-Ray Photoelectron Spectroscopy (XPS)<sup>13</sup>, Scanning Electron Microscopy (SEM)<sup>14</sup>, or ex-situ Solid-State Nuclear Magnetic Resonance (SSNMR)<sup>15</sup>, are dealing with the technical difficulties of handling the minute, fragile SEI population, risking that the fundamental nature of SEI might be damaged during the destructive process.

NMR spectroscopy is quantitative (the signal is proportional to the number of detected atoms in the system), versatile (many elements can be detected, in liquid, solid or heterogeneous phases), non-invasive and non-destructive. These valuable advantages, combined with its ability to track ultra-fast processes, make NMR spectroscopy a supreme characterization tool that can provide information about the structure and dynamics of the system with chemical sensitivity. NMR offers various sequences and

observables, allowing the integration of multiple methodologies to study a given system at multiple resolutions. In this research, we used  $^6\text{-}^7\text{Li}$  isotope labeling and CEST NMR to study the ionic transport of Li across the interface. The ion transport is considered a multistage process involving the separation of Li ions from their solvation sheath in the electrolyte, Li diffusion through the SEI phase, and exchange between the SEI and the metal anode (*Figure 2*). As mentioned, the last subprocess, i.e., the solid-solid interaction between the SEI and the metal phases, is often overlooked in the research community; this is possibly due to the technical challenges of characterizing this process and the fact that processes under OCV conditions draw less attention in general. In previous studies, Ilott & Jerschow<sup>16</sup> and Gunnarsdóttir et al.<sup>17</sup> have used  $^6\text{-}^7\text{Li}$  isotope exchange to investigate Li transport. We continue their efforts as we believe this NMR methodology is still far from reaching its full potential. However, this technique inherently lacks the resolution to differentiate the subprocesses mentioned of the transport, resulting in data representing the overall effect. Therefore, to understand better the ion transport, we used CEST NMR, focusing solely on the Li metal||SEI solid-solid interaction.

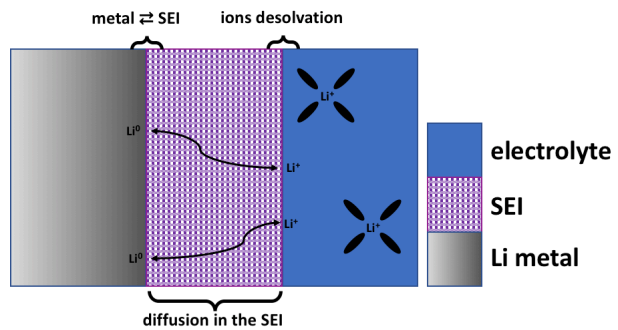


*Figure 2: a scheme showing the subprocesses associated with Li transport: desolvation of Li ions in the electrolyte, diffusion through the SEI layer, and exchange between the SEI and the metal phases.*

## 4. Objectives

In this thesis, we intended to study Li metal||SEI||electrolyte systems by integrated research involving original experimental and computational approaches. By taking advantage of the NMR's versatility, these systems were investigated by two methods, each highlighting different aspects of the ionic transport process:

### 4.1 Investigate SEI properties by CEST

We aimed to develop a CEST methodology to probe ion dynamics across metal||SEI||electrolyte interface, focusing on Li metal||SEI solid-solid interaction.

### 4.2 Modeling interfacial Li exchange process at OCV

We aimed to expand the use of  $^6\text{-}^7\text{Li}$  isotope labeling methodology by optimizing the experimental setup and designing a robust & intuitive numerical model of the system.

### 4.3 Thesis structure (a general comment for the reader)

The thesis consists of two separate projects: the CEST project (*chapter 5*) and the isotope exchange project (*chapter 6*), each of which can be read independently. I chose this structure because, despite the conceptual similarity of the projects, each is based on a completely different theory, experimental methodology, data processing, and modeling approach. Thus, trying to unify these two projects into one single story can lead to confusion and lack of coherence. Note that each project has its *conclusion & outlook* section.

## 5. CEST

### 5.1 Motivation and approach

In light of the challenges associated with the SEI research, finding a tool with the sensitivity to detect the minute SEI population, *and* has the required resolution to differentiate between all of the dynamic interfacial processes, is of great importance. Therefore, the efforts should be focused on both system design and the development of characterization methodology. As mentioned, Li dendrites are one of the most significant factors that inhibit the industrial use of Li metal batteries, and the number of studies (experimental and theoretical) dedicated to solving the problem is increasing annually. However, we understand that what makes Li dendrites a cause for failure in a battery cell can be exploited for research purposes. Due to their fractal nature, Li dendrites present a set of unique physical properties, especially the high surface area<sup>18,19</sup>, which turns them into a desirable model system that can be used for various measurements and experiments.

Here, we present a novel combination of system & methodology to investigate and quantify the exchange process at the Li metal||SEI interface. The system of choice is Li metal dendrites formed under electrochemical conditions, suspended in a Li salt electrolyte. The methodology of choice is CEST, a well-known NMR technique originally used in liquid- and protein-NMR<sup>20,21</sup>. The primary advantage of using Li dendrites as a system for CEST experiments is their high specific surface area (SA), estimated in  $>13.5\text{m}^2/\text{mol}$ ,  $\sim 200$  times higher than a macroscopic piece of Li metal (see Appendixes for calculations); theoretically, 3d fractals have infinite surface area. In this context, high SA means increasing the total number of Li atoms in the SEI and, consequently, the total number of Li atoms that participate in the interfacial dynamic processes. Therefore, the SA is a crucial factor as it is directly correlated with the observable CEST effect. Another significant advantage, which also stems from the unique geometry of the dendrites, is that the skin depth is not an issue since NMR detection includes all of the Li atoms in the dendrites<sup>3</sup>.

So, what can the CEST experiment teach us about the properties of the SEI? In general, the technique provides information regarding the chemical exchange interaction between different pools of nuclei, so it can be used to determine whether such interaction exists and how many environments are interacting. Furthermore, using theoretical CEST models allows quantification of these interactions, i.e., extraction

of exchange rates and population ratios of the pools. Specifically, CEST gives an indication regarding the interaction between Li atoms in the metal and Li ions in the SEI, therefore providing insights regarding the physical properties of the SEI. In this project, we used these experimental and theoretical tools to compare between systems of Li dendrites covered with different types of SEI.

## 5.2 Experimental

### 5.2.1 Materials

Electrolytes: (i) 1M LiPF<sub>6</sub> in 1:1 v/v ethylene carbonate/dimethyl carbonate (EC/DMC; Sigma Aldrich; commercial name: LP30). (ii) LP30 + FEC: fluoroethylene carbonate (FEC; Sigma Aldrich; 99%) were added to LP30 electrolyte in 1:9 ratio by volume (LP30 + FEC). (iii) 1M LiTFSI in 1:1 v/v DOL/DME was made by dissolving LiTFSI salt (dried under vacuum for 48 hours; Sigma Aldrich) in DOL (1,3-Dioxolane; Sigma Aldrich) and DME (Dimethoxymethane; Sigma Aldrich). Li electrodes were prepared by cutting fresh <sup>7</sup>Li (Sigma; 99.9% trace metal basis). All materials were kept and handled in an Ar atmosphere glovebox (O<sub>2</sub>, H<sub>2</sub>O < 0.5 ppm).

### 5.2.2 Li dendrites formation

Two rectangular fresh <sup>7</sup>Li metal pieces (~0.02 cm<sup>2</sup>; <1mg) were cut using scissors and adhered onto Pt wires in a specially designed electrochemical device (*Figure S1*). 200μl of electrolyte was added to a standard 5mm NMR tube. The electrochemical device was inserted into the NMR tube, such that the Li pieces were fully immersed in the electrolyte, forming a symmetrical Li||Li cell. A constant current of 0.5mA, corresponding to ~25mA/cm<sup>2</sup>, was applied to the cell for 4 hours (*Figure S1*). Then, the electrochemical device (with the Li metal pieces) was removed from the NMR tube and the grey, fluffy, Li metal dendrites were left suspended in the electrolyte. The tube was sealed and taken to the NMR measurements.

### 5.2.3 NMR

NMR measurements were done on a Bruker Avance III 9.4T spectrometer, operating at a Larmor frequency of 400 MHz for <sup>1</sup>H and 155.5 MHz for <sup>7</sup>Li. The spectra were recorded on a 5mm BBI probe. The pulse duration was calibrated for each measurement separately (corresponding to a flip angle of 90° and ~17μs). Recycle delay was set to 8s allowing the probe to cool down from the saturation pulses. T<sub>1</sub> relaxation times of Li metal and Li electrolyte were measured using inversion recovery experiment, and T<sub>2</sub> values were measured using CPMG pulse sequence. The spectra were processed in Bruker Topspin software, using the automatic phase, baseline correction, and peaks integration. Further data processing was performed in MATLAB. Measurements were performed at three temperatures: 298K, 310K and 323K.

## 5.3 Theory

CEST is commonly used as a contrast mechanism in magnetic resonance imaging (MRI) and protein NMR to follow transient or low-populated “invisible” states<sup>20,21</sup>. The CEST effect is based on having a



large pool of nuclei (typically the water protons) exchanging with a low population that resonates at a different frequency. The exchange process and the resonance of the low population site can be determined by following the change in the large population resonance after saturating the transition of the low population. In the  $^7\text{Li}$  NMR spectrum of Li metal immersed in electrolyte (Figure 3), the signals of the metal and the diamagnetic Li (i.e.,  $\text{Li}^+$  in the electrolyte and SEI) are well separated ( $\sim 40\text{kHz}$ ), such that the difference between the peaks in Hz is much larger than the exchange rate, being an advantage for CEST. In heterogeneous systems containing both solid and liquid (e.g., Li metal + electrolyte), the CEST effect can be increased by controlling three main factors: (i) increasing the absolute surface area of the solid, (ii) maximizing the surface to volume ratio, and (iii) controlling the exchange rate by raising the temperature. The formalism used to quantify the CEST results was developed by Zaiss et al. and is described in detail here<sup>22</sup>. In general, the results of CEST experiments are visualized in Z-spectra; in a Z-spectrum, the magnetization of the saturated water,  $M_{\text{sat}}(\Delta\omega)$  (normalized as a fraction of the unsaturated water magnetization,  $M_0$ ), is plotted as a function of the saturation frequency  $\omega$ . Since the acquired signal  $S_{\text{sat}}$  or  $M_0$  is proportional to the magnetization, the normalized Z-spectrum is described by the value  $Z(\Delta\omega)$  which is defined as follow:

$$[1] Z(\Delta\omega) = \frac{S_{\text{sat}}(\Delta\omega)}{S_0} = \frac{M_{\text{sat}}(\Delta\omega)}{M_0}$$

The evaluation of the CEST signal is done by using two Z-values: the label scan,  $Z_{\text{lab}} = Z(\Delta\omega = +\delta\omega_b)$ , which is the normalized Z-magnetization after saturation at the CEST resonance, and the reference (or control) scan, representing the saturation without CEST effect that can be estimated from the opposite frequency ( $Z_{\text{ref}} = Z(\Delta\omega = -\delta\omega_b)$ ). Then, the CEST effect can be defined by the magnetization transfer ratio asymmetry (MTR<sub>asym</sub>), given by:

$$[2] \text{MTR}_{\text{asym}} = \frac{M_{\text{sat}}(-\delta\omega_b)}{M_0} - \frac{M_{\text{sat}}(+\delta\omega_b)}{M_0}$$

However, this equation was developed for CEST in liquids, and hence it is assumed that the detected signal from the main pool (usually water) consists of potentially exchangeable nuclei (due to the fast diffusion in the liquid). In systems where the main pool is a solid phase (i.e., Li metal), this assumption does not hold as the diffusion in the solid is considerably slower, so the detected signal from the metal does not necessarily originate from exchangeable nuclei solely. Roughly, the metal signal can be divided into *exchangeable fraction*, composed of Li atoms in the first few atomic layers close to the surface, and *unexchangeable fraction* corresponding to Li atoms in the bulk that are not exchanging yet contributing to the signal intensity. The CEST effect is defined as an interaction between at least two exchangeable pools; therefore, in cases where the exchangeable fraction is small, the measurable effect is *lower* than the actual effect (and sometimes invisible). Furthermore, quantification of the effect becomes more problematic due to the challenge of determining the value of the exchangeable fraction. To account for the exchangeable fraction, denoted as  $f_{\text{exchangeable}}$ , Eq. [2] needs to be modified:

$$[3] MTR_{asym} = \frac{M_{sat}(-\delta\omega_b) - (1 - f_{exchangeable}) \cdot M_0}{M_0 - (1 - f_{exchangeable}) \cdot M_0}$$

$$- \frac{M_{sat}(+\delta\omega_b) - (1 - f_{exchangeable}) \cdot M_0}{M_0 - (1 - f_{exchangeable}) \cdot M_0} = \frac{M_{sat}(-\delta\omega_b) - M_{sat}(+\delta\omega_b)}{f_{exchangeable} \cdot M_0}$$

With the physical constrain:

$$M_{sat}(-\delta\omega_b) - M_{sat}(+\delta\omega_b) \leq f_{exchangeable} \cdot M_0$$

Reflecting that the size of the effect could not exceed the size of the pool itself. In other words, it is impossible to have a CEST effect bigger than 100%.

#### 5.4 Results

We first show that CEST effect is barely observed in bulk Li + electrolyte system. Given that Li atoms are undergoing spontaneous  $\text{Li}^0 \rightleftharpoons \text{Li}^+(\text{e}^-)$  exchange process at room temperature conditions<sup>16</sup>, it is particularly surprising: neither CEST “directions”, i.e., saturating the diamagnetic signal while detecting the metal signal, nor saturating the metal while detecting the diamagnetic Li, have

provided any significant effect (Figure 3). It is noteworthy, that the same results were obtained after many different tries and experimental configurations. We hypothesize that the physical geometry of the Li metal chunk is diminishing the CEST effect in two ways: (i) lowering the absolute surface area, i.e., decreasing the amount of exchange sites, and (ii) lowering surface-to-bulk ratio, leading to a smaller fraction of exchangeable Li atoms in the metal signal, and hence decreasing the theoretical upper limit of the

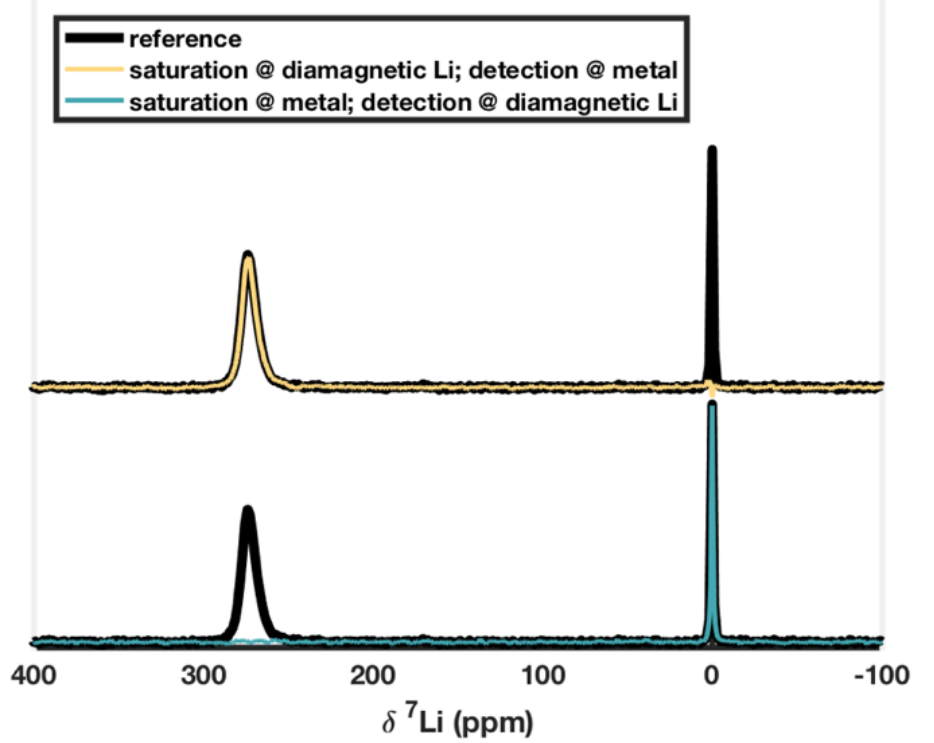


Figure 3: Results of CEST experiment on Li metal + LP30 electrolyte, visualized in  $^7\text{Li}$  NMR spectrum of the system. In the reference curve (in black), the peaks at  $\sim 0\text{ppm}$  (corresponds to diamagnetic Li) and  $\sim 260\text{ppm}$  (metal) can be observed. (power level of saturation: 500Hz; saturation time: 1sec; 298K)

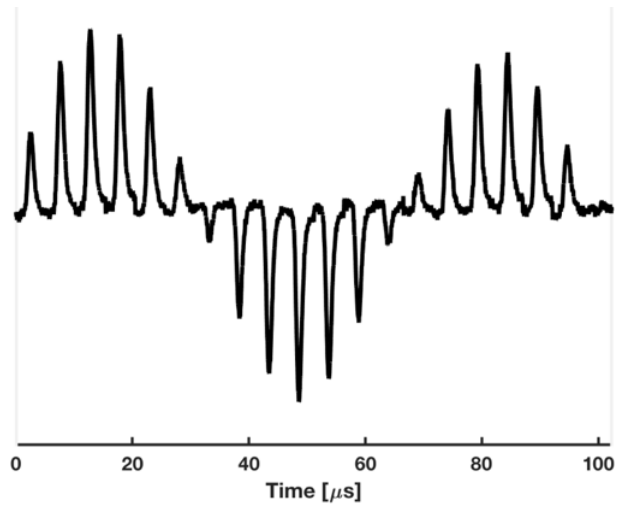


Figure 4: nutation curve of Li dendrites acquired at an RF of 14.7 kHz.

observable effect. Gladly, the problems associated with Li metal chunks do not apply for Li dendrites as their specific SA is almost 2-3 orders of magnitude higher (see Appendixes). In Li dendrites, the number of potential exchange events is significantly increased as well as their surface-to-bulk ratio. *Figure 4* shows a nutation curve of the Li dendrites, where the intensity is plotted as a function of the duration of the RF pulse. The prolonged sine periodicity indicates that all the Li atoms in the dendrites are fully excited and subsequently detected and quantified by the NMR measurement, ensuring that the maximal thickness of the dendrites is no more than 1-2 microns<sup>3</sup>. Therefore, it is assumed that for Li dendrites,  $f_{exchangeable} \approx 1$ , meaning that all of the atoms in the dendrites are considered as exchangeable. For a more detailed discussion regarding the estimation of  $f_{exchangeable}$  in Li dendrites, see Appendixes.

#### 5.4.1 Quantification of exchange rate using varying saturation power (QUESP)

In the QUESP experiment, the CEST effect is quantified according to Eq. [3], where the varied parameter is the power level of the saturation pulse. In general, increasing the power level means increasing the range of frequencies that are being saturated by the pulse, as well as the extent of saturation, both resulting in a larger fraction of the signal being saturated. Therefore, the CEST effect

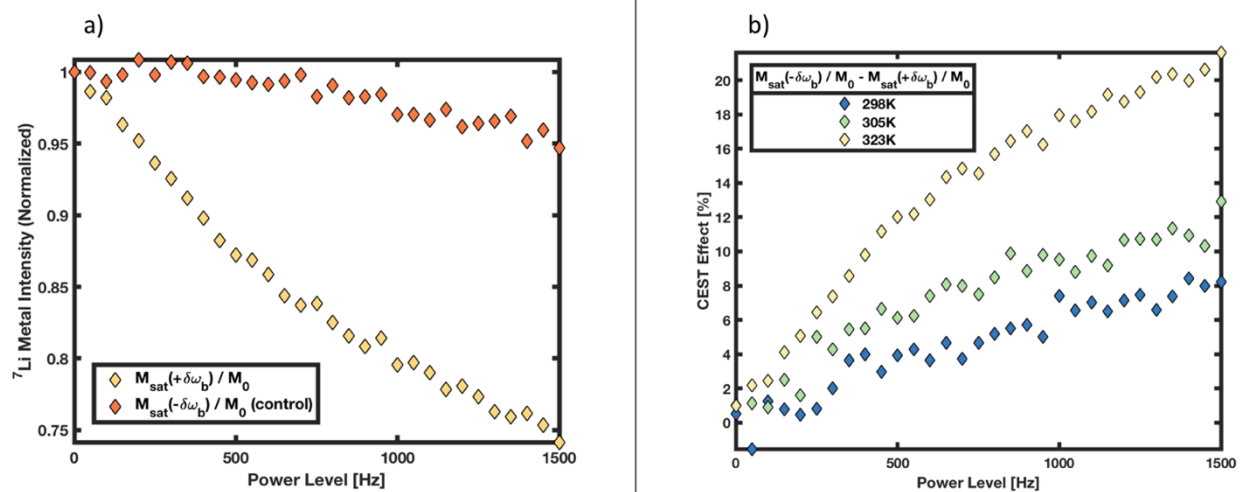


Figure 5: results from QUESP experiment on Li dendrites + LP30 electrolyte. Raw data of the measurement is plotted in (a), where the different curves represent the CEST measurement and the control measurement. In (b), CEST effect is plotted for three different temperatures. The legends of the curves are explained according to Eq. [2]. Saturation time: 200ms, 323K.

is increased with the power level. *Figure 5* shows the results of QUESP experiment done on Li dendrites immersed in LP30 electrolyte. The raw data can be seen on the left side (a): the yellow data points represent the (normalized) intensity of the metal signal after saturating the frequency of diamagnetic Li, and the orange data points represent the reference, or control measurements, where the saturation was done at the opposite offset (Eq. [2]). The decrease shown in the control measurement is explained by the instantaneous heating of the metal immediately after the RF pulse was applied. On the right side (b), CEST effect is plotted as a function of power level in three different temperatures. As expected, the CEST effect increases at higher temperatures since the exchange rate is temperature dependent following Arrhenius equation.

### 5.4.2 Z-spectra

In Z-spectra, each data point represents the (normalized) metal intensity plotted as function of the saturation offset. Phrased differently, this experiment can be understood as a “scanner”, where a certain range of frequencies (around the peak of interest) is scanned, and according to the response (i.e., the y-

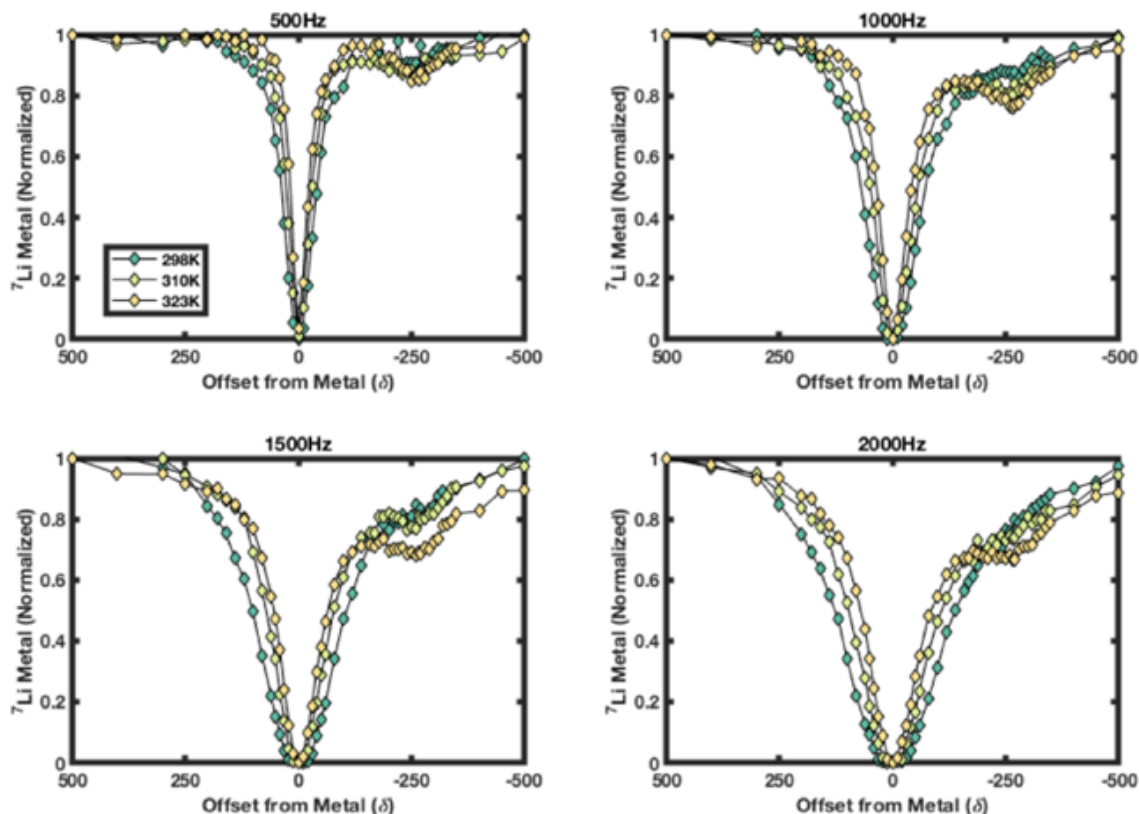


Figure 6: Z-spectra of Li dendrites + LP30 electrolyte; each subplot represents set of measurements at different power level power of saturation (see titles of the subplots), and each curve represents different temperature (see legends). The saturation time was 200ms

axis) it can be determined whether there is an exchangeable environment at that particular frequency. Generally, a deviation from the symmetric shape of the central dip indicates there is an interaction with this environment. *Figure 6* shows results from a set of CEST measurements, visualized as Z-spectra. The dip emerging at offset  $\sim 260$  ppm suggests an exchange process between the environments of Li metal and diamagnetic Li. There are clear trends that can be observed in the data: the size of the CEST effect, i.e., the depth of the dip at  $\sim 260$  ppm, is more significant at higher temperatures (as already seen in the QUESP experiments), indicating higher exchange rates. In addition, interestingly, the dip at  $\sim 260$  ppm gets broader with increased temperature while the dip of the metal gets narrower with temperature. This may imply on opposite trends in the  $T_2$  relaxation properties of the corresponding environments. For the single-phase metal, the increased mobility with temperature leads to longer  $T_2$  and narrower line shape. As for the diamagnetic environment, we assume (as will be explained in the next section) that it corresponds to Li in the multiphase solid structure of the SEI. Hence, it is reasonable

that there is an intrinsic Li exchange within this pool, and that the exchange rate is increased with temperature. Therefore, the broadening may be due to the increased exchange within the SEI phases

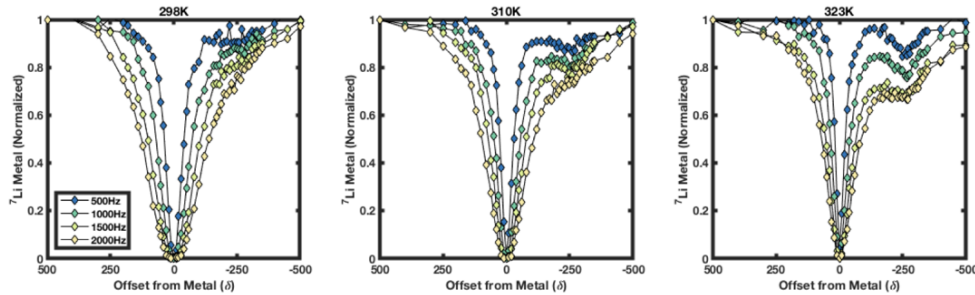


Figure 7: Z-spectra of Li dendrites + LP30 electrolyte; each subplot represents set of measurement at different temperature (see titles of the subplots), and each curve represents measurement different power level (see legends). The saturation time was 200ms.

which could either lead to broadening due to exchange between phases with shorter relaxation times or due to additional phases in the SEI, which vary in their chemical shift, contributing to the CEST effect. Figure 7 shows the same experimental data visualized in slightly different way, emphasizing the effect of the power level; it can be seen that the direct saturation is more significant at higher power levels, as explained, reflected in broadening of the metal dip.

#### 5.4.3 $Li_{metal}^0 \rightleftharpoons Li_{electrolyte}^+$ or $Li_{metal}^0 \rightleftharpoons Li_{SEI}^+$ ?

One of the most important questions to address in this project was to determine what is measured in the CEST experiment. The answer to this question is not trivial as the  $Li^+$  environments in both electrolyte and SEI phases are overlapping (around ~0ppm in  $^7Li$  NMR spectrum, or ~-260ppm in the Z-spectra). Thus, practically, it is difficult to say which environment interacts with the metal, and this limitation prevents answering the research question, let alone providing useful insights regarding the system. However, there are two major reasons for the argument that the measured exchange is between the metal phase and the SEI phase:

- I. *Figure 8* shows a z-spectrum of Li-dendrites in LP30 electrolyte. The upper and the lower plots are the (normalized) integrated intensities of metal and electrolyte peaks, respectively. The areas colored with green gradients represent the level at which the *electrolyte* was saturated such that darker green means offsets with higher saturation and lighter green with lower saturation efficiency. Now, the fact that only a minor fraction of CEST effect in the *metal* is colored means that the saturation of the electrolyte cannot be responsible to the observable effect. Furthermore, no decrease in electrolyte signal is observed where the metal is saturated (around offset 0), implying that there is no direct interaction between these two environments.
- II. As can be seen from the QUESP experiment (*Figure 5*), the CEST effect increases with the power level. Saturation with higher power levels means broadening the range and efficiency of the saturation. Since the relatively narrow electrolyte signal is fully saturated at very low power levels (*Figure 9*), the increase of the effect has to be due to an exchange with the much broader and harder to saturate (and apparently invisible) resonances of the diamagnetic Li in the SEI.

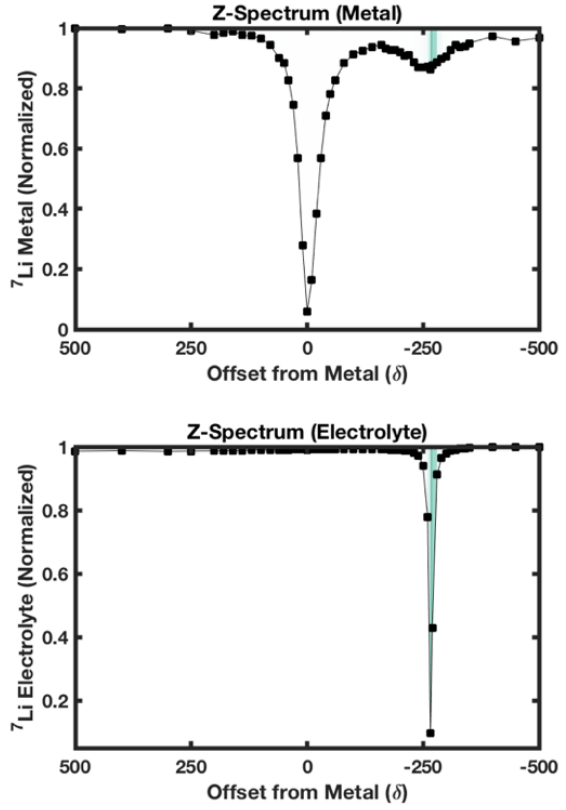


*Figure 8: Z-spectrum of Li dendrites + LP30 electrolyte (power level: 500Hz, 323K). The metal and electrolyte intensities are shown in the upper and the lower plots, respectively.*

For these reasons, we argue that the observable relation between the metal and electrolyte signals is incidental and does not imply an exchange process between these two pools, and that the observed effect is due to the interaction between the metal and the SEI phases. To the best of our knowledge, this is the first time that the CEST technique is being applied to a system of two solids.

#### 5.4.4 Fitting

In collaboration with Prof. Moritz Zaiss, the experimental data was fitted using a modeling approach that is described in detail here<sup>23,24</sup>. The fitting results will be presented in a later publication.

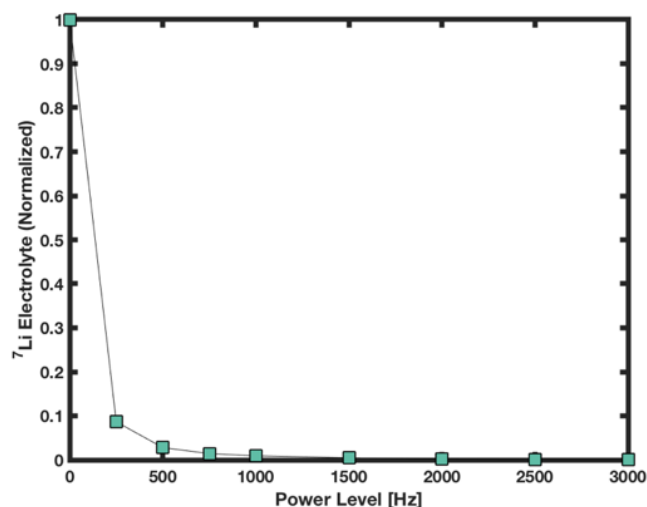


Figure 9: QUESP experiment on Li dendrites + LP30 electrolyte. The intensity of the electrolyte is plotted as a function of the power level.

#### 5.5 Conclusions & outlook

We believe that this project involves three aspects of innovation, in terms of the system that was investigated, the NMR technique, and also new insights regarding the materials:

- i. Viewing Li dendrites as a *tool* that can be used to expand the NMR's range of possibilities, instead of a *problem* that needs to be solved.
- ii. Providing proof-of-concept for solid-solid CEST, for the first time.
- iii. Characterizing SEI physical properties, including metal $\rightleftharpoons$ SEI exchange rate and density of the SEI's inner layers.

The project opens the way for many other systems that can be studied by CEST, e.g., dendrites made from other metals (Na, Mg, Zn, etc.) formed in the presence of different types of electrolytes.

## 6. Li isotope exchange

### 6.1. Motivation and approach

In the past, isotopic labeling has been used to investigate the kinetics at the Li metal electrolyte interface with NMR<sup>16,17</sup>. This approach takes advantage of the fact that different isotopes are similar in their chemical behavior yet distinctive in their magnetic resonance properties. Therefore, by controlling and manipulating the initial fractions of isotopes in different components in the system, it is possible to track how these fractions change with time as isotopes diffuse within the system. Using this method, we can study heterogeneous systems that include a pristine <sup>6</sup>Li metal piece (95% <sup>6</sup>Li enriched) immersed in three different electrolytes: (i) LiPF<sub>6</sub> in 1:1v EC: DMC (or in its commercial name: LP30), (ii) LP30 + FEC additive (9:1v) and (iii) LiTFSI in 1:1v DME:DOL - all containing natural abundance Li (92%



$^7\text{Li}$ ). By measuring the  $^7\text{Li}$  intensities of the distinctive signals of the metal ( $\sim 260\text{ppm}$ ) and the electrolyte ( $\sim 0\text{ppm}$ ) over time, we can directly monitor the system dynamics.

In a closely related project, we investigated Li metal anodes that were coated with artificial single-component SEIs. Theoretically, this is an ideal way to isolate factors and characterize the behavior of each type of SEI component separately<sup>25,26,27</sup>. In collaboration with Prof. Betar Gallant from MIT, we investigated the Li transport properties of several different artificial coatings. Thus, we expected to determine which SEI phases are beneficial (i.e., chemically stable and ion-permeable) for transport and which are not. For example, LiF is considered a beneficial phase, and its presence in the SEI has been correlated with an improved performance of Li metal cells<sup>28</sup>.

It is important to note that all measurements were done at open-circuit voltage (OCV), assuming that understanding the system at OCV is a precondition to understanding the much more complicated system that operates under voltage.

## 6.2. Three time-dependent processes

The dynamics of the system are controlled by three different physical processes where each significantly dictates the trends in the observable measurements (scheme of the processes is shown in *Figure 10*):

### 6.2.1. Li ion exchange

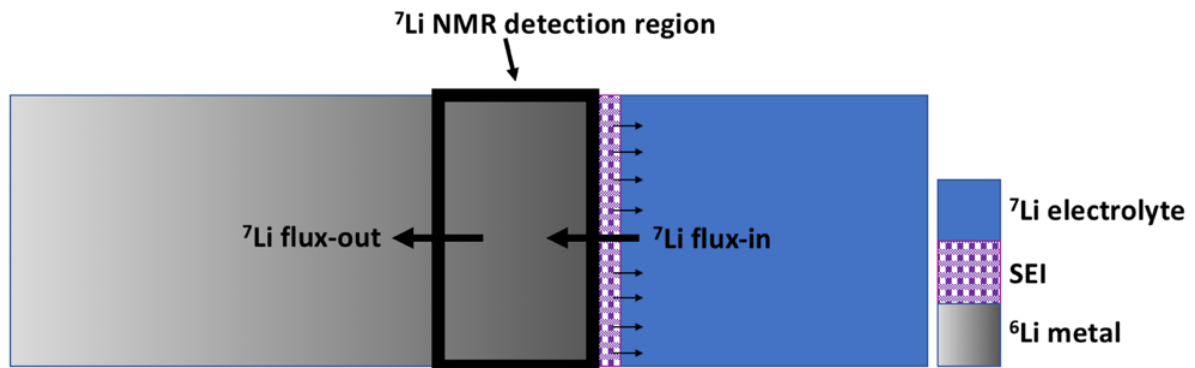
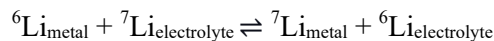


*Figure 10: a scheme showing the three processes that affect the measured data: (i) exchange at the interface, (ii) SEI formation, and (iii) self-diffusion of Li atoms in the bulk.*

At room temperature, Li ions have enough thermal energy to exchange between the solid (Li metal) and liquid (electrolyte) phases. However, this steady state process is unobservable if the isotopic fractions in the two phases are the same. Therefore, introducing significant differences in the initial isotopic fractions allows a simple observation of the exchange process, that can be described by:



As already mentioned, the so-called “Li-ion exchange” is, in fact, a combination of three different subprocesses: Li-ion desolvation, diffusion through the SEI, and exchange between the SEI and the metal (*Figure 2*).



### 6.2.2. Corrosion (native SEI formation)

As mentioned, once the Li metal and electrolyte are in contact, the corrosion process starts due to the extreme reactivity of Li metal. As a result, electrolyte species decompose on the metal surface, forming an interphase layer known as the native SEI. The SEI growth is a time-dependent process that seemingly modifies the rate and the path by which Li-ions exchange between the solid and the liquid across the interface.

### 6.2.3. Self-diffusion of Li metal atoms

In the beginning, Li isotopes are uniformly distributed within the metal (95%  $^6\text{Li}$ , 5%  $^7\text{Li}$ ). During the exchange process, the metal surface is loaded with a relatively large amount of  $^7\text{Li}$  atoms, thereby breaking the uniform distribution of isotopes. These concentration gradients are then gradually equilibrated by the spontaneous diffusion process at which  $^7\text{Li}$  atoms start to diffuse towards metal bulk (where the  $^7\text{Li}$  fraction is low). Due to the skin effect, the NMR detection is limited and characterized by the skin depth,  $\delta$ , a constant used to determine the distance to which the RF radiation can effectively penetrate inside the metal bulk<sup>29,30,31</sup>. Simply put, the NMR is sensitive only to the surface of the metal and a few microns inside it. Thus, from the perspective of NMR detection, a flux of  $^7\text{Li}$  atoms comes in (from the electrolyte), and a flux goes out towards the metal bulk (*Figure 10*). Importantly, the self-diffusion process does not directly affect the transport (unlike exchange and corrosion) but significantly affects the detected NMR signal and, therefore, must be accounted for.

## 6.3. Experimental

### 6.3.1. Sample preparation

The setup for the measurements was similar to previous works.  $^6\text{Li}$  metal was cut using an oval punch resulting in a metal piece with size of 15mm x 2.8mm, and mass of ~10mg. The piece was inserted into an NMR tube (5mm Medium Wall Low Pressure/Vacuum NMR tube, 7”) and 200 $\mu\text{l}$  of electrolyte was added. Then, quickly as possible, to minimize the time between the sample preparation and measurement, the sample was taken to the NMR. The time gap between addition of electrolyte and acquisition of the first NMR data point was *ca.* 30 minutes and was later taken into account in the numerical simulations.

### 6.3.2. NMR

NMR measurements were done on a Bruker Avance III 9.4T spectrometer, operating at a Larmor frequency of 400 MHz for  $^1\text{H}$  and 155.5 MHz for  $^7\text{Li}$ . The spectra were recorded on a 5mm BBI probe. The sample was oriented such that the Li metal long axis was parallel to the  $B_0$  field and perpendicular to the  $B_1$  field. The pulse duration was calibrated for each measurement separately (corresponding to a flip angle of  $90^\circ$  and ~17 $\mu\text{s}$ ), with a recycle delay of 0.8s chosen such that the metal resonance is fully relaxed between scans ( $T_1$  of  $^7\text{Li}$  metal ~150ms) and 320 transients recorded. This resulted in a total sampling time of the exchange process of 256s. The spectra were processed in Bruker Topspin software,

using the automatic phase, baseline correction, and peaks integration. Additional data processing was performed in MATLAB. All measurements were performed at 298K.

### 6.3.3. Self-diffusion experiment

After ~24 hours of measurement, the sample was taken out from the NMR and put back in the gloves-box. To remove any traces of Li electrolyte, the sample was washed several times in a solvent (DMC for LP30 and LP30/FEC and DME for LiTFSI) followed by drying under vacuum in the pre-chamber for ~15 minutes. Then, the dried Li metal piece was taken out again to be measured in the NMR, similar to the description above.

### 6.3.4. Coated samples

The samples were made in the group of Prof. Betar Gallant (MIT), using a methodology described in detail here.<sup>32,33</sup> The samples that were measured included the following: (i) pristine  ${}^6\text{Li}$ , (ii)  ${}^6\text{Li}||\text{LiF}$ , (iii)  ${}^6\text{Li}||\text{Li}_2\text{O}$  (lithium oxide), (iv)  ${}^6\text{Li}||\text{LiEG}$  (lithium ethylene glycol), (v)  ${}^6\text{Li}||\text{ROCO}_2\text{Li}$ . The NMR measurements were done on a 400MHz Bruker system with a static probe, at 295K.

## 6.4. Model

### 6.4.1. Motivation

As described, the experimental data is affected by three physical processes: ion exchange, corrosion/SEI formation, and self-diffusion of Li metal atoms. All of these processes occur at similar time scales and are proven to be significant factors. In this case, simple qualitative interpretation of the results can be misleading and provides very rough conclusions. Therefore, to unlock the full potential of the isotope exchange methodology, the experimental technique must be coupled to an appropriate model used to accurately “deconstruct” these three processes and determine, quantitatively, the contribution of each to the observable trends. In the past<sup>16,17</sup>, multiple efforts have been made to model similar systems, and these previous works undeniably inspire the model that will be described here. Nevertheless, in this model, some modifications were made, and several key issues were addressed:

1. Simple and intuitive model.
2. Adding the self-diffusion experiment:
  - a. Represents only the process of self-diffusion that is isolated from the other factors.
  - b. Increases the robustness and the level of validation of the model; more data is fitted using fewer fitting parameters.
3. Careful implementation of NMR detection (i.e., the skin effect).

### 6.4.2. Agent-based modeling using NetLogo

The model was developed as a hybrid of equation-based modeling (EBM) and agent-based modeling (ABM)<sup>34</sup>. ABM is generally considered a “bottom-up” approach where the system's elementary components are modeled as objects (or *agents*), having a set of properties and rules defining their behavior. These rules usually concern short-range interactions (i.e., with other agents in the close

neighborhood). ABM is mainly used in modeling complex systems that are too complicated to be captured by equations only.<sup>35</sup> Conversely, EBM is a “top-down” approach, where analytical expressions are derived from first principles to yield a set of equations that describe, usually in a continuous manner, the system's behavior in time and space. Phrased differently, in ABM, the ontology is at the individual level (i.e., the agent), whereas in EBM, the ontology is at the global level. Through a combination of ABM and EBM, the model has the flexibility to deal with the heterogeneous nature of this complex system while allowing implementation and integration of the existing knowledge regarding the dynamics (in the form of deterministic kinetic and diffusion equations). To be more specific, the *system* is defined in ABM terminology, whereas the *interactions* are defined in terms of EBM. The model was developed in NetLogo<sup>36</sup>, a platform designed for ABM, and hence is mainly used for this kind of modeling. The choice of using NetLogo (over Python/MATLAB, for example) was made in light of the following advantages:

1. A well-developed, interactive GUI; straight forward & intuitive visualizations.
2. Netlogo's *diffuse* built-in function:
  - i. Simulating 1,2,3-dimensional diffusion problems in a single line of code; trivial setting of boundary and initial conditions.
  - ii. Straightforward relations between the input parameters of *diffuse* and the analytical expressions of the physical equations.
  - iii. Computationally efficient.
3. Built-in calibration toolbox (using GA / RandomSearch / Simulating Annealing optimization algorithms).

### 6.4.3. The model

#### 6.4.3.1. Work assumptions

The primary guideline of the model is simplicity: the model aims to capture the most with the least amount of assumptions and degrees of freedom.

Unless otherwise specified, the following will be assumed:

1. 1-dimensional problem: the spatial changes of the relevant processes (exchange, corrosion, diffusion) occur along a single axis perpendicular to the metal surface. The model assumes zero gradients with respect to the other axes. Thus, the model is trivially converted to a 3-dimensional problem as it is directly proportional to the 1-dimensional problem.
2. Instantaneous diffusion of the liquid: the diffusion of Li ions in the liquid is ~5 orders of magnitude faster than in the metal, therefore considered instantaneous.
3. The number of moles of Li in the SEI (including other soluble species) is negligible compared to the metal and the electrolyte.
4. Given assumption (3), the system is isolated, so the total amount of Li is conserved across the system.

### 6.4.3.2. System definition

Figure 11 shows a scheme of the system in the model. The system is represented as a 1-dimensional spatial grid of  $n$  cells (or *patches* in NetLogo's jargon); each patch acts as an individual object with its own identity, properties (e.g., the fraction of  $^7\text{Li}$ ), and rules of interactions (i.e., exchange, diffusion). Three types of patches were defined per their spatial locations:

1. *Electrolyte (E)*: represents the electrolyte object in the system, interacts with its neighboring patch, the metal surface patch ( $M_{interface}^0$ ). According to assumption (2) above, the isotopic fractions are uniform everywhere in the liquid, so a single object can sufficiently describe the electrolyte behavior.

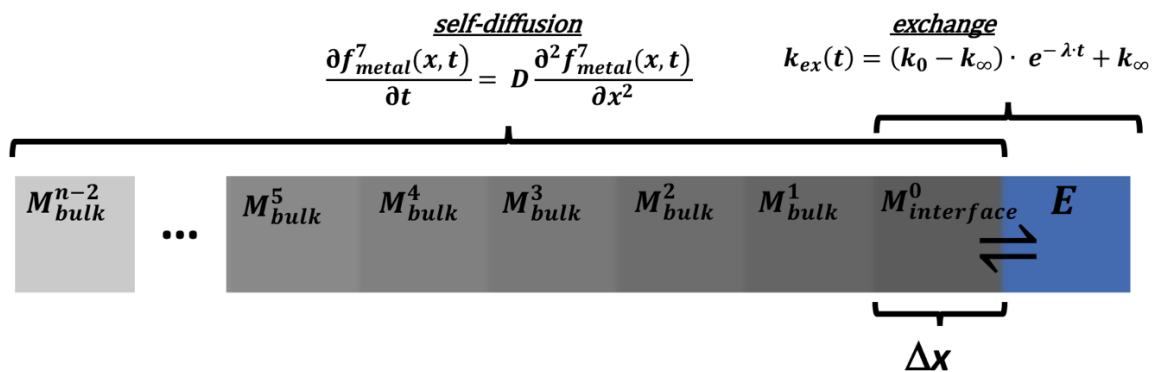


Figure 11: a cartoon showing the different components (objects) in the system, and the main interactions between them: the exchange at the interface is described by Eq. [7], and the self-diffusion by Eq. [8]. The shading color of the metal objects is demonstrating the diffusion of  $^7\text{Li}$  atoms towards the bulk.

2. *Metal bulk* ( $M_{bulk}^1$  to  $M_{bulk}^{n-2}$ ): represent Li metal bulk objects where the upper subscripts denote their spatial location.
3. *Metal interface* ( $M_{interface}^0$ ): represents the metal interface object, interacts with the electrolyte  $E$  and with  $M_{bulk}^1$ .

At each time step ( $\Delta t$ ) in the simulation, the following occur:

1. The time-dependent interactions are calculated.
2. The objects interact with their adjacent neighbors according to Eq. [7] and Eq. [8].
3. The properties of the objects are updated (i.e.,  $^7\text{Li}$  fraction).
4. The system is “measured” to yield the simulated data points.
5.  $t = t + \Delta t$  (then back to 1.).

### 6.4.3.3. Interactions

#### 6.4.3.3.1. Ion exchange at the interface

The SEI formation process,  $L(t)$ , in units of length, can be modeled in exponential form:

$$[4] L(t) = L_{\infty} \cdot (1 - e^{-\lambda \cdot t})$$

Where  $L_{\infty}$  is the maximal and final thickness of the layer and  $\lambda$  is a decaying constant, in units of  $\text{s}^{-1}$ , representing the rate at which the corrosion process slows down. Consequentially, the change in the SEI formation, i.e., the corrosion rate, is as follow:

$$[5] \frac{dL}{dt} = r_{corrosion} = r_{corrosion}(t=0) \cdot e^{-\lambda \cdot t}$$

This equation expresses the assumption that the corrosion process stops (i.e., the metal is passivated) after some time. It is important to note that this process is governed by kinetics considerations rather than thermodynamics ones.<sup>9</sup> Theoretically, Li metal atoms should keep reacting with the electrolyte until one of the reagents is entirely consumed due to the extreme reactivity of Li, which is far from the electrolyte stability window. However, the probability that electrons will flow through the insulating SEI decreases as the layer grows and gets thicker. Similarly, theoretically, the exchange flux should proceed until the system reaches isotopic balance in metal and electrolyte, which is, again, far from what experimentally observed. Therefore, to explain the observable trends, it will be assumed that the exchange flux of Li ions is time-dependent and decreases as a function of the SEI thickness.

The exchange flux, in units of  $mole \cdot sec^{-1} \cdot m^{-2}$ , is of the form:

$$[6] j_{ex}(t) = \frac{k_{ex}(t) \cdot n_{Li}}{SA}$$

Where  $k_{ex}(t)$ , in units of  $s^{-1}$ , is the exchange rate,  $n_{Li}$  is the total number of Li moles in the metal surface patch ( $M_{surface}^0$ ), and  $SA$  is the surface area of the sample. The expression for  $k_{ex}(t)$  takes the form of Newton's law of cooling:

$$[7] k_{ex}(t) = (k_0 - k_{\infty}) \cdot e^{-\lambda \cdot t} + k_{\infty}$$

Where  $k_0$  is the initial exchange rate and  $k_{\infty}$  is the exchange rate when the SEI has reached its maximal thickness (i.e.,  $L_{\infty}$ ). The exponential term expresses the dependency of the exchange on the corrosion process. For the derivation of  $k$  and its relation to NetLogo's built-in *diffuse*, see Appendixes.

#### 6.4.3.3.2. Self-diffusion

To describe the self-diffusion of Li atoms within the metal, the 1-dimensional diffusion equation is used:

$$[8] \frac{\partial f_{metal}^7(x, t)}{\partial t} = D \frac{\partial^2 f_{metal}^7(x, t)}{\partial x^2} \quad 0 < x < d$$

Where  $f_{metal}^7(x, t)$  is the fraction of  $^7Li$  in the metal,  $D$  is the diffusion coefficient, and  $d$  is the half thickness of the metal. The boundary condition at the surface is:

$$\frac{\partial f_{metal}^7(0, t)}{\partial x} \approx \frac{f_{elec}^7(t) - f_{metal}^7(0, t)}{\Delta x}$$

Where  $\Delta x$  is the spatial interval defined in the model. In the bulk, due to the symmetric boundary condition at  $x=d$ :

$$\frac{\partial f_{metal}^7(d, t)}{\partial x} = 0$$

For a detailed explanation regarding the relation between the built-in *diffuse* function and the analytical form of the diffusion equation, see Appendixes.

#### 6.4.3.3.3. Setting $k_{ex}$ to zero

The self-diffusion experiment is easily implemented in the simulation as after a chosen number of time steps, corresponding to the actual experimental time,  $k_{ex}$  is set to zero, i.e., no exchange flux. The (sub)system of the metal patches then becomes isolated from the electrolyte and the B.C.s are changed to:

$$\frac{\partial f_{metal}^7(0, t)}{\partial x} = \frac{\partial f_{metal}^7(d, t)}{\partial x} = 0$$

#### 6.4.3.4. NMR detection

The experimental data is not a reflection of the physical system but how the NMR “sees” the physical system. The theory used to quantify the detected NMR signal of the Li metal was developed by Bhattacharyya et al.<sup>3</sup> For a radiofrequency (RF) field of strength  $\omega_1$ , the effective field inside the metal at spatial depth  $x$  from the metal surface is given by:

$$[9] \quad \omega(x) = \omega_1 \cdot e^{-\frac{x}{\delta}}$$

$\delta$ , the skin depth, is calculated:

$$[10] \quad \delta = \sqrt{\frac{\rho}{\pi \mu_0 \mu_r \nu}} = 10.47 \mu m$$

Where  $\rho$  is the resistivity of the metal ( $94.7E-09 \Omega \cdot m$  for Li metal at 298K),  $\mu_0$  is the vacuum permeability of ( $12.56E-07 m \cdot kg / s^2 \cdot A^2$ ),  $\mu_r$  is the relative permeability of the medium (1.4 for Li metal), and  $\nu$  is the frequency of the applied rf field in this research (155.5 MHz). For direct excitation NMR experiments, the NMR signal intensity ( $S$ ) is related to  $\omega_1$  and duration of the rf pulse ( $\tau_p$ ), via  $S \propto \sin(\omega_1 \tau_p)$ . To maximize the signal intensity,  $\tau_p$  is chosen to satisfy  $\omega_1 \tau_p = \pi/2$ . Therefore, inside the metal,  $\omega_1$  decreases as a function of depth, and  $\omega_1$  is replaced by  $\omega(x)$  (Eq. [9]):

$$[11] \quad S \propto \int_0^{\infty} \sin(\omega(x) \tau_p) dx$$

In this research, the half thickness of the metal ( $\sim 200 \mu m$ ) is far greater than the skin depth ( $10.47 \mu m$ ), and therefore the upper limit of the integral can be set to infinity. Numerically, the NMR signal over time was calculated by the inner product of the vectors  $\sin(\omega(x) \tau_p)$  and  $f_{metal}^7(x, t)$ .

#### 6.4.3.5. Implementing the surface area of the metal in the model

To account for the ratio between moles of Li in the *electrolyte* patch and in the *metal interface* patch, an additional proportionality constant was defined,  $SA\_factor$ , such that:

$$[12] \quad SA\_factor = \frac{n_{electrolyte}}{n_{metal\ interface}}$$

The number of moles of Li in the interface layer is given by:

$$[13] n_{metal\ interface} = \frac{V_{interface\ layer} \cdot \rho_{Li}}{MW_{Li}} = \frac{SA \cdot \Delta x \cdot \rho_{Li}}{MW_{Li}}$$

Where  $\rho_{Li}$  (0.534 g/cm<sup>3</sup>) is the metal density,  $MW_{Li}$  (6.06 g/mol) is the molecular weight,  $SA$  is the geometrical surface area of the sample ( $\sim 0.85$  cm<sup>2</sup>), and  $\Delta x$  (2E-04 cm) is the spatial interval (i.e., the patch size) in the simulation. The number of Li moles in the electrolyte is 200E-06mol, therefore:

$$SA\_factor = \frac{n_{electrolyte}}{n_{metal\ interface}} \cong 13.2$$

Notably, since the exchange rate and the surface area are inversely proportional (Eq. [6]), underestimation of the surface area will cause an overestimation in the exchange flux. For sensitivity analysis of the model to the value of surface area, see Appendixes.

#### 6.4.3.6. Model setup

The model was calibrated using NetLogo's built-in application *BehaviorSearch*.<sup>37</sup> The process was done by optimizing three fitting parameters:  $k_0$ ,  $k_\infty$ , and  $\lambda$ . The error function chosen to fit the simulations to the experimental data is MSE (mean squared errors). Practically, the value to minimize was the total MSE for all three measurements such that:

$$MSE_{total} = MSE_{metal} + MSE_{electrolyte} + MSE_{self-diffusion}$$

where each measurement has an equal weight in the total error. The search algorithm that was used is the Genetic Algorithm. Each dataset (i.e., LP30, FEC, or LiTFSI) was optimized in 20 independent searches to provide a valid statistical analysis of the fitting. Mean and standard deviation values were calculated for the best four searches (for a detailed explanation, see Appendixes). The list of input parameters that were used in the simulation are shown in *Table 1*:

$\Delta x$ [m]	2E-06
$\Delta t$ [s]	16
$D_{metal}$ [m <sup>2</sup> /s]	7.11E-15
Initial fraction of <sup>7</sup> Li - electrolyte	0.92
Initial fraction of <sup>7</sup> Li - metal	0.05
Skin depth ( $\delta$ ) [m]	10.47E-06
Half thickness of the metal [m]	200E-06
Surface area [m <sup>2</sup> ]	8.5E-05 $\pm$ 0.1E-05
$k_0$ [Hz]*	8.0E-07 – 4.0E-04
$k_\infty$ [Hz] *	0 – 4.0E-05
$\lambda$ [Hz] *	0 – 6.25E-04

\*fitting parameters

Table 1: list of fixed and fitting parameters used in the simulation. The values for the fitting parameters are the lower and upper bounds used in the model calibration

## 6.5. Results

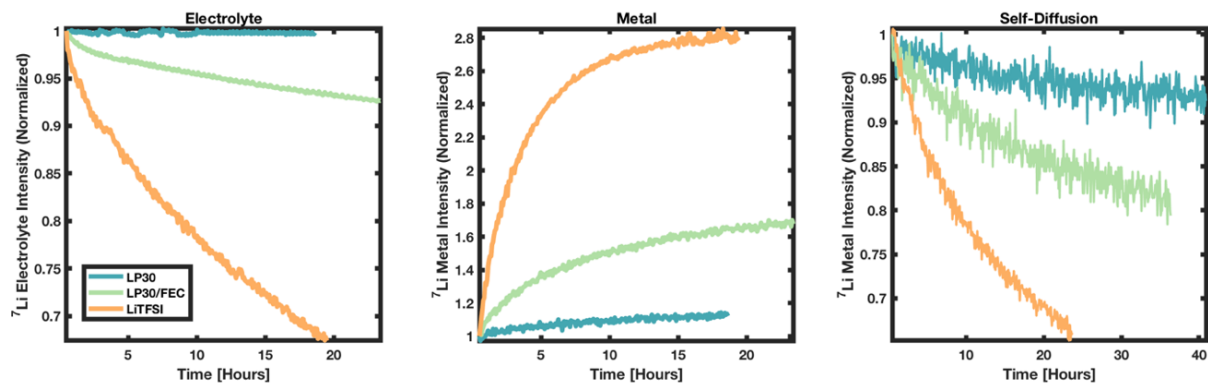


Figure 12: data of isotope exchange and self-diffusion experiments for three different systems of metal + electrolyte: (i)  ${}^6\text{Li}$  + LP30, (ii)  ${}^6\text{Li}$  + LP30/FEC, and (iii)  ${}^6\text{Li}$  + LiTFSI. Results of the exchange experiment are presented in the left and the middle subplots: integrated intensity of  ${}^7\text{Li}$  is plotted vs time for the electrolyte peak (left) and metal peak (middle). Results of the self-diffusion experiment are presented in the right subplot where the integrated intensity of  ${}^7\text{Li}$  metal is plotted vs time.

### 6.5.1. Experimental Results

Experimental curves are presented in Figure 12. Each data point represents the (normalized) intensity of the metal/electrolyte signal.

The general trends: due to spontaneous Li-ion exchange and the fact that the initial fractions of isotopes are significantly different in each phase, the intensity of  ${}^7\text{Li}$  in the  ${}^6\text{Li}$ -enriched metal is increasing while the electrolyte intensity is decreasing, as shown in Figure 13. As can be seen, the electrolyte in LP30 shows almost no decrease. A possible explanation could be that  $T_1$  of the electrolyte gets shorter with time. The data was collected with a relatively short relaxation delay of 0.8s, which is not sufficient for

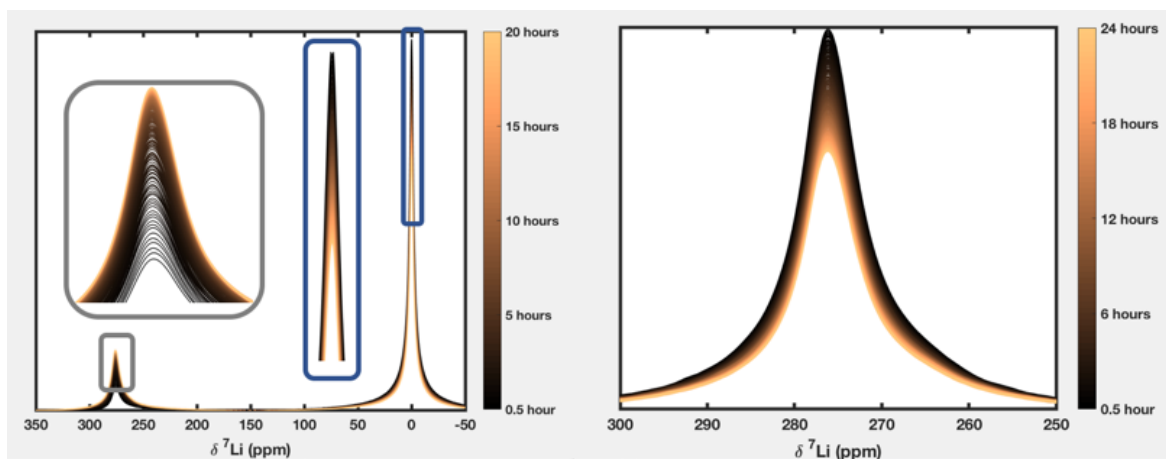


Figure 13: results of ion exchange (left) and self-diffusion (right) experiments, from the perspective of the NMR spectrum. In the exchange experiment, the signal intensity of the electrolyte is decreasing with time while the metal signal is increasing. In the self-diffusion experiment, the signal intensity of the metal is decreasing with time due to self-diffusion of Li atoms in the bulk.

electrolyte full relaxation. In case the relaxation time of the electrolyte shortens, its relative signal will get more intense, compensating for the decrease due to isotope exchange. Therefore, the actual decrease of the electrolyte should be more significant, as suggested by the simulation's results (see next section). In the self-diffusion experiments, the decrease of  ${}^7\text{Li}$  intensity is explained by the flux-out of  ${}^7\text{Li}$  atoms



beyond the NMR detection region (Figure 10). Similar to previous observations, the variance between different electrolyte systems is significant, meaning that the dynamics at the interface (corrosion & exchange) are unique for each system. In addition, it can be seen that the relative size of the effect is consistent across all measurements, such that  $\text{LiTFSI} > \text{LP30/FEC} > \text{LP30}$ . However, due to the time dependency of the exchange in the corrosion process, it is hard to extract insights regarding the underlying mechanisms from qualitative examination of the data.

### 6.5.2. Simulation fitting

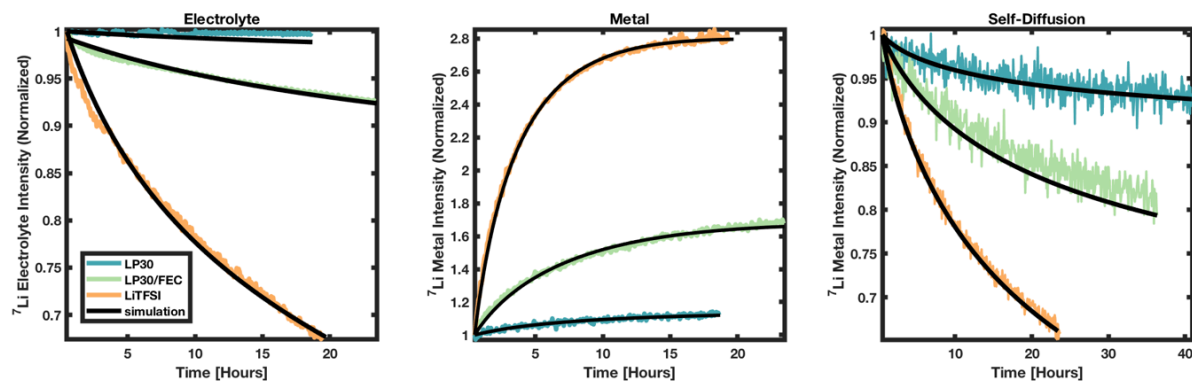


Figure 14: Experimental data of isotope exchange and self-diffusion measurements plotted with the fitted simulation curves.

Visually, it can be seen that model describes the experimental data pretty well, capturing metal, electrolyte, and self-

	LP30	FEC	LiTFSI	ratios LP30:FEC:LiTFSI
$k_0$ [Hz]	1.81E-06	8.83E-06	1.09E-04	$\sim 1 : 5 : 60$
$k_{\infty}$ [Hz]	7.63E-07	1.84E-06	3.86E-05	$\sim 1 : 2.5 : 50$
corrosion constant [Hz]	2.43E-05	1.81E-05	3.83E-05	$\sim 1 : 0.75 : 1.5$
MSE	3.09E-04	7.10E-04	4.59E-04	

Table 2: fitted values determined from the model.

diffusion datasets simultaneously (Figure 14). The fitted values ( $k_0$ ,  $k_{\infty}$ ,  $\lambda$ ), including the goodness of fitting (MSE) for each set of measurements, are summarized in Table 2. For stability and error analysis of the fitting parameters, see Appendixes.

### Corrosion

An important aspect regarding the SEI is the question when the system is passivated, meaning how much time it takes until the interface is chemically stable. To address this question, the fitted values of the corrosion decaying constant,  $\lambda$ , were converted to the time the SEI has reached 95% from its maximal length (using Eq. [4]). According to the fitting, the passivation time takes  $\sim 22$  hours for LiTFSI electrolyte, and  $\sim 45$  hours for LP30/FEC, suggesting that the passivation process in LiTFSI is significantly faster. These values were found to be numerically stable and statistically significant (Table S1). For LP30, the fitted value of  $\lambda$  has a relatively large error leading to a passivation time in range of  $\sim 19$ -38 hours. This may indicate that a more complex process occurs at the interface.

### Exchange

The expression for  $j_{ex}(t)$ , i.e., the exchange flux at the interface at any point in time, can be extracted from the model (fitted  $j_{ex}(t)$  for the three systems can be found in the Appendix). However, the values of  $k_0$  and  $k_\infty$  are more indicative as they represent intrinsic physical properties of the system, and the values were found to be numerically stable and statistically significant (Table S1). According to the fitting,  $k_0$  in LiTFSI system is  $\sim 60$  times higher than in LP30 and  $\sim 10$  times higher than in LP30/FEC.  $k_0$ , the initial exchange rate where there is no SEI, could indicate the desolvation process which is separating Li ions from their solvation sheath in the electrolyte. This process is considered the bottleneck of the ion transport process as it requires more energy than the diffusion in the SEI and the solid-solid exchange between the SEI and the metal.<sup>38</sup> Interestingly, after full passivation, the ratios are slightly changed as  $k_\infty$ , the exchange rate at the maximal thickness of SEI is  $\sim 50$  times higher in LiTFSI than LP30 and  $\sim 25$  times higher than LP30/FEC. We hypothesize that the factor of desolvation is more significant than diffusion through the SEI and the metal||SEI exchange.

### 6.5.3. Generalization of the model

To demonstrate that the model is generalizable, the experimental data generated by Gunnarsdóttir et al. was fitted by our model. As can be seen (Figure 15), the model captures the datasets successfully. It can be seen that the fitted values for  $j_{ex}$  in both models are very similar (Table 3) despite the

differences in the implementation of the NMR detection, at which the model was found to be sensitive to (see Appendixes for more details). Nevertheless, such proximity in the results can also be used as a validation for both models.

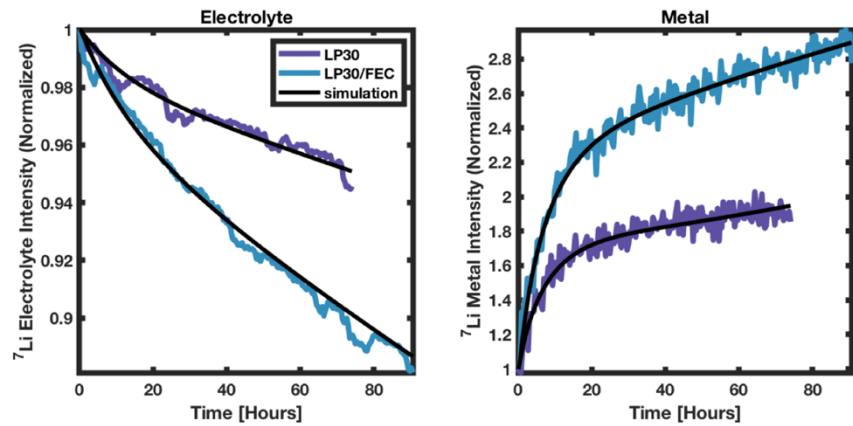


Figure 15: data of ion exchange experiment generated by Gunnarsdóttir et al., plotted with the simulated curves fitted by our model.

$j_{ex} [\text{mole} \cdot \text{sec}^{-1} \cdot \text{m}^{-2}]$	Model	Gunnarsdóttir et al. <sup>17</sup>
$j_{ex(t=0)} \text{ LP30}$	1.8E-06	1.6E-06
$j_{ex(t=74\text{hrs})} \text{ LP30}$	0.51E-06	0.49E-06
$j_{ex(t=0)} \text{ LP30/FEC}$	3.4E-06	3.1E-06
$j_{ex(t=74\text{hrs})} \text{ LP30/FEC}$	1.2E-06	1.2E-06

Table 3: comparison of values fitted by the model of Gunnarsdóttir et al., and by our model.

### 6.5.4. Coated samples – collaboration with MIT

Figures 16,17 present results of ion exchange measurements on different samples, where the increase of  $^7\text{Li}$  metal intensity is plotted on the left subplot and the decrease of  $^7\text{Li}$  electrolyte is plotted on the

right. Despite having some difficulties in this project, two qualitative observations are of some importance:

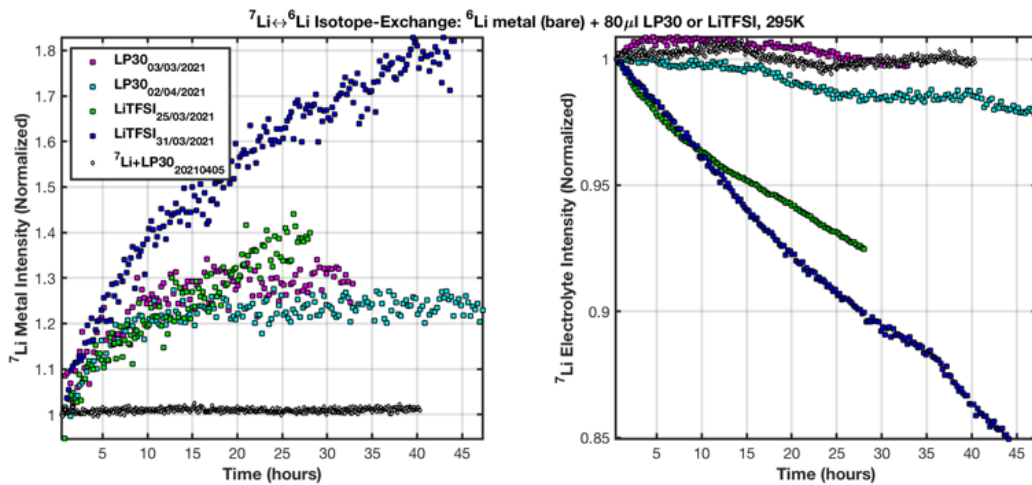


Figure 16: results of isotope exchange experiments of pristine  ${}^6\text{Li}$  metal immersed in two  ${}^7\text{Li}$  electrolytes, LP30 and LiTFSI.  ${}^7\text{Li}$  metal immersed in LP30 was done as a control experiment.

1. LP30 electrolyte behaves very poorly in the presence of Li metal compared to LiTFSI that has been shown to improve the exchange (Figure 16). This trend was observed almost in all measurements across all projects.
2. Surprisingly,  ${}^6\text{Li}||\text{LiEG}$  showed some promising potential, as it presented the fastest exchange observed among all samples that were measured in this project (Figure 17). We believe this coating should be a subject of further investigation.

The experimental challenges stemmed from three major reasons: First, the thickness of the coating was found to be a significant factor in the exchange behavior. Without the ability to control the formation process of the coatings in sufficient control over the coating thickness or provide an accurate measurement for the

thickness obtained – the variance within the groups (i.e., samples with the same coating but with unknown thicknesses) was more significant than the variance between the groups (i.e., samples with

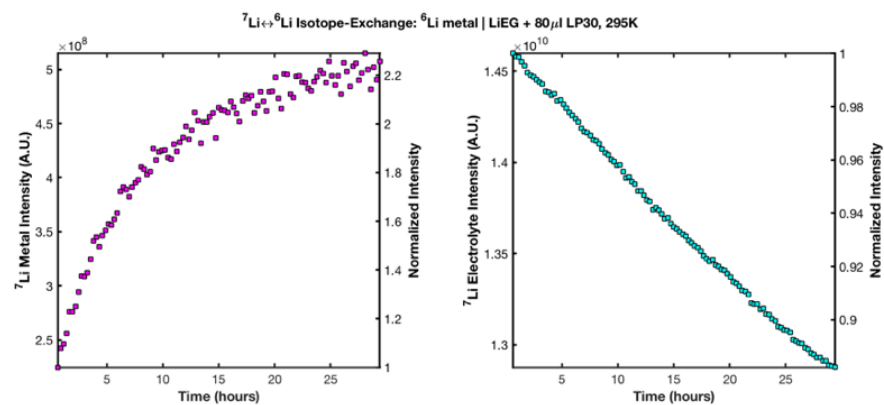


Figure 17: Experimental results of isotope exchange of  ${}^6\text{Li}$  metal coated with LiEG immersed in  ${}^7\text{Li}$  LP30 electrolyte.

different types of coatings). Thus, we could not provide any quantitative conclusion regarding different chemistries of the SEI. Second, it was observed that at the first round of measurements, the exchange was much faster compared to the next ones. One explanation may be that the samples were degraded in the glove box in some unexpected way, such that their interface behavior was modified. Lastly, the problematic setup: the coil did not contain the whole sample, such that not all of the electrolyte was in

the detection region. As a result, artifacts in the measurements were observed, especially regarding the electrolyte data.

## 6.6. Conclusions & outlook

Li isotopic labeling is a simple and elegant methodology to track interfacial dynamics in Li metal||SEI||electrolyte systems, processes that currently cannot be tracked in any other way. Using the advantages of NMR, the generated experimental data has high quality, which allows easy comparison of different systems. In addition, the self-diffusion experiment was performed to increase the level of validity of the experimental data. The dynamical systems were quantified through a numerical model, yielding unique sets of fitted values used to describe the corrosion and interfacial exchange processes. The results suggest that LiTFSI electrolyte presents the fastest Li transport compared to LP30 and LP30/FEC (~50 times faster than LP30 and ~25 times faster than LP30/FEC, after full passivation). Assumingly, this is due to lower desolvation energy rather than faster diffusion in the SEI or faster metal $\rightleftharpoons$ SEI exchange.

The model developed as ABM/EBM hybrid was shown to be both interpretable and general and stands as proof of concept that this modeling approach can be an ideal combination of simplicity and interpretability without making significant compromises. We believe that this kind of modeling can be extended to many other complex systems that physical chemists investigate.

## 7. Appendixes

### 7.1. CEST

#### 7.1.1. Li dendrites formation

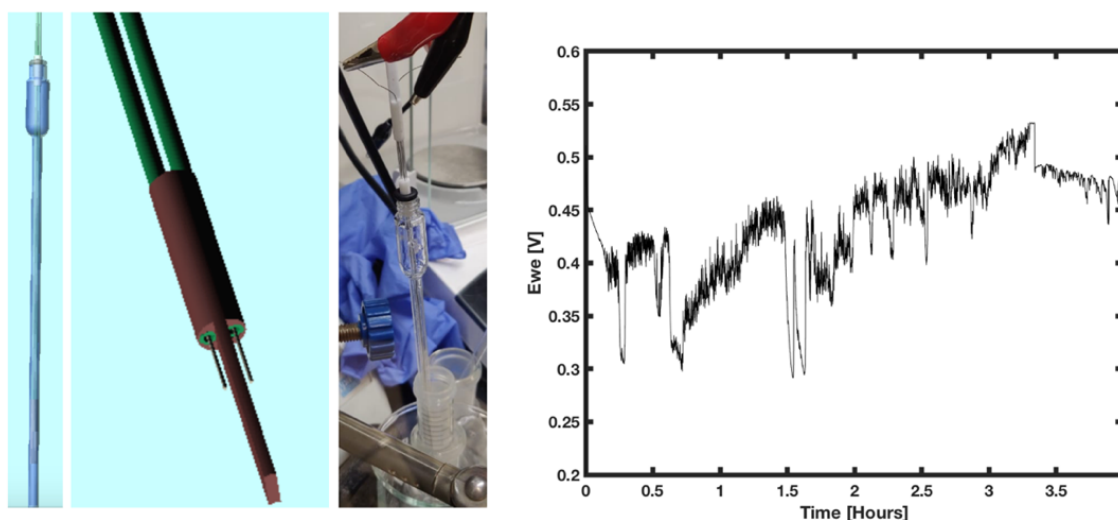


Figure S1: the electrochemical device used to form Li dendrites (left), and an example for electrochemical profile of the process, where the potential is plotted as function of time (right). This profile corresponds to dendrites formation in a fractal geometry (see ref. 4).

### 7.1.2. Estimating the surface area of Li dendrites

To extract the numerical values of the physical parameters of interest, an estimation of the surface area (SA) of the dendrites is required. The CEST effect (i.e., the fraction of the total signal that is decreased due to exchange interaction with a saturated pool) is correlated with the number of exchange events occurring during the saturation pulse. The number of events can be written such that:

$$\# \text{ of exchange events} \propto k_{ex} \cdot SA$$

Meaning, the exchange rate and the surface area are inversely proportional to one another in terms of the CEST effect, such that any uncertainty in the estimation of the SA directly affects the confidence in the value of  $k_{ex}$ . To estimate the SA of dendrites, we used a method that involves NMR relaxation measurements<sup>39</sup>.  $T_1$  and  $T_2$  relaxation values were measured (inversion recovery for  $T_1$ ; CPMG for  $T_2$ ) on four different samples: (i) LP30 electrolyte; (ii) LP30 + 1 Li metal piece; (iii) LP30 + 3 Li metal pieces; (iv) LP30 + Li dendrites. The Li dendrites were formed by an electrochemical process where a constant current was applied in a symmetrical Li metal cell. The Li metal pieces were cut by an oval punch to produce fixed size pieces. In samples (ii)-(iv), the same amount of electrolyte was added, and the samples were kept in the gloves-box for ~24h to let the SEI formation finish and stabilize.

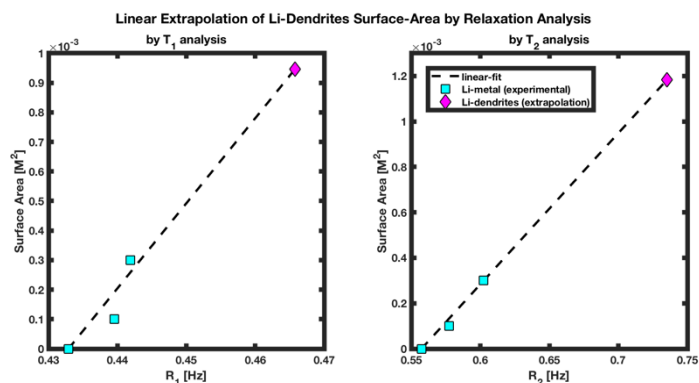


Figure S2: results from relaxation analysis

According to Equation (3) in the paper<sup>39</sup>, SA of the solid is linear with the relaxation rate, so a line can be fitted using three data points of samples (i)-(iii) (where both relaxations and SA values are known), and estimate the SA of sample (iv) by extrapolation. The equation that was used to fit was simply  $SA = a \cdot R_{1,2} + b$ . The results from the experiment are shown in Figure S2. It can be seen from the plots that the SA of the dendrites is ~10-times higher than the SA of 1 Li metal piece (by taking the mean value of the two analysis).

To find the specific SA (i.e. per mole of Li), the SA values were divided by the number of Li moles in the sample. The number of Li moles in a metal piece:

$$n_{Li-piece} = \frac{mass}{MW} = \frac{10 \cdot 10^{-3} g}{6.941 \frac{g}{mol}} = 1.4 \cdot 10^{-3} mol$$

The number of Li moles in the dendrites is calculated by taking the electrochemical parameters that were used to form the dendrites, assuming no deposition on the electrodes at all (i.e. every Li ion that is reduced contributes to the dendrites that were collected and measured):

$$n_{dendrites} = \frac{I \cdot time}{F} = \frac{0.5 \cdot 10^{-3} \frac{C}{sec} \cdot 14,400 sec}{96485 \frac{C}{mol}} = 7.4 \cdot 10^{-5} mol$$

Thus, the specific SAs are given by:

$$SA_{Li-metal} = \frac{measured\ SA}{n_{Li-piece}} = \frac{1 \cdot 10^{-4} m^2}{1.4 \cdot 10^{-3} mol} \cong 7.1 \cdot 10^{-3} \frac{m^2}{mol}$$

$$SA_{dendrites} = \frac{extrapolated\ SA}{n_{dendrites}} = \frac{1 \cdot 10^{-3} m^2}{7.4 \cdot 10^{-5} mol} \cong 13.5 \frac{m^2}{mol}$$

We can see that dendrites have specific SA that is almost 200 times higher than Li metal. This is with agreement with the results in previous research<sup>40</sup> where it was concluded that SA of a cycled Li metal anode is about 150 times higher than the geometric SA.

### 7.1.3. Estimating the fraction of Li atoms on the surface of Li dendrites

To address this question, we first estimate the number of Li moles that cover a given area. We can provide a very rough (yet rationalized) estimation by simply using Li metal density. From the value of the density we can extract values of 1d and 2d Li metal densities. Assuming a perfectly symmetrical Li metal cube in size of 1cm, and in volume of 1ml, the number of Li atoms per volume is given by:

$$\frac{density}{MW} \cdot N_A = \frac{0.534 \frac{g}{cm^3}}{6.941 \frac{g}{mol}} \cdot 6.022 \cdot 10^{23} \frac{atoms}{mol} = 4.63 \cdot 10^{22} \frac{atoms}{cm^3}$$

For 1d density:

$$\frac{atoms}{m} = \sqrt[3]{4.63 \cdot 10^{22} \frac{atoms}{cm^3} \cdot 100 \frac{cm}{m}} = 3.6 \cdot 10^9 \frac{atoms}{m}$$

Now, 2d density in terms of moles per area:

$$density_{2d} = \frac{(3.6 \cdot 10^9 \frac{atoms}{m})^2}{N_A} = \frac{1.29 \cdot 10^{19} \frac{atoms^2}{m^2}}{6.022 \cdot 10^{23} \frac{atoms}{mol}} = 2.15 \cdot 10^{-5} \frac{mol}{m^2}$$

To estimate the number of Li moles at the surface of a metal piece:

$$n_{surface}^{Li\ piece} = density_{2d} \cdot SA = 2.15 \cdot 10^{-5} \frac{mol}{m^2} \cdot 1 \cdot 10^{-4} m^2 = 2.15 \cdot 10^{-9} mol$$

To estimate the number of Li moles at the surface of the dendrites:

$$n_{surface}^{dendrites} = density_{2d} \cdot SA = 2.15 \cdot 10^{-5} \frac{mol}{m^2} \cdot 1 \cdot 10^{-3} m^2 = 2.15 \cdot 10^{-8} mol$$

Finally, the fraction of Li atoms on the surfaces can be calculated:

$$f_{Li\ piece\ surface} = \frac{n_{surface}^{Li\ piece}}{n_{Li\ piece}} = \frac{2.15 \cdot 10^{-9} mol}{1.4 \cdot 10^{-3} mol} \approx \mathbf{1/650000}$$

$$f_{Li\ dendrites\ surface} = \frac{n_{surface}^{dendrites}}{n_{dendrites}} = \frac{2.15 \cdot 10^{-8} mol}{7.4 \cdot 10^{-5} mol} \approx \mathbf{1/3000}$$

Theoretically, it can be assumed that the fraction of Li atoms on the dendrites surface is proportional to the fraction of the exchangeable site, which in turn dictates the observable CEST effect. However, experimentally, we get that the reduction of the signal in the CEST experiment can reach up to 30% and even more, meaning that the *actual* exchangeable fraction is *at least*  $0.3 = 1 / 3.33 \gg 1 / 3000$ . There are several reasons that could explain this gap:

1. The SA of the dendrites was underestimated: In the calculation it was assumed that the actual SA of the Li metal piece is the geometric SA, so any deviation from this will linearly affect the value of SA for the dendrites.
2. The total number of Li moles in the dendrites was overestimated: Probably, this value should be lower since during the electrochemistry some of the Li was required for the SEI formation and/or deposited on the Li metal electrode.
3. The diffusion of Li atoms within the dendrites is very fast (due to increased number of structural defects), so bulk Li atoms are also actively participating in the CEST.

#### 7.1.4. QUESP of Li dendrites + Li metal bulk

To emphasize the difference in CEST effect between dendrites and metal piece, we measured QUESP on a sample of Li dendrites + Li metal electrodes. *Figure S3* shows a comparison between two samples, with and without Li metal pieces: We can clearly see that adding bulk Li pieces decreased the CEST effect significantly. The reason for this is that out of the total signal of the Li pieces, only a tiny fraction of it is actually taking part in the exchange process. Therefore, there is a fixed fraction of the Li-metal signal that is “embedded” in the measurement, and yet does not contribute to the effect at all. These findings strengthen the argument that Li-dendrites is the preferable system for CEST measurements.

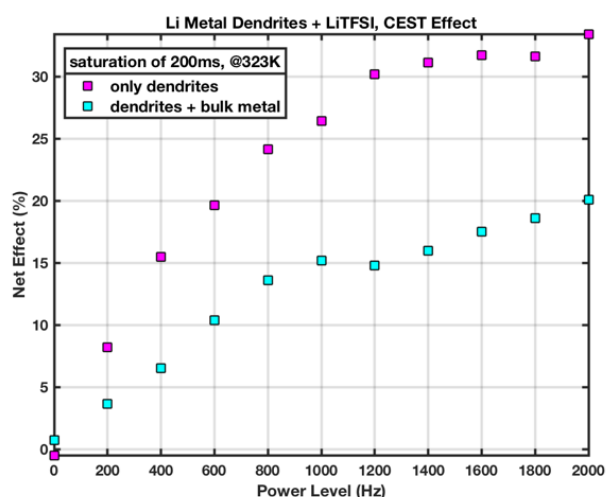


Figure S3: QUESP on Li dendrites (magenta) and Li dendrites + bulk Li metal (cyan)

## 7.2. Isotope exchange

### 7.2.1. NetLogo's *diffuse* function

Description from NetLogo's official documentation:

#### **diffuse patch-variable number**

Tells each patch to give equal shares of (*number* \* 100) percent of the value of *patch-variable* to its eight neighboring patches. *number* should be between 0 and 1. Regardless of topology the sum of *patch-variable* will be conserved across the world. (If a patch has fewer than eight neighbors, each neighbor still gets an eighth share; the patch keeps any leftover shares.) Note that this is an observer



command only, even though you might expect it to be a patch command. (The reason is that it acts on all the patches at once -- patch commands act on individual patches.)

An example:

```
diffuse chemical 0.5
;; each patch diffuses 50% of its variable chemical to its neighboring 8
;; patches. Thus, each patch gets 1/8 of 50% of the chemical from each
;; neighboring patch
```

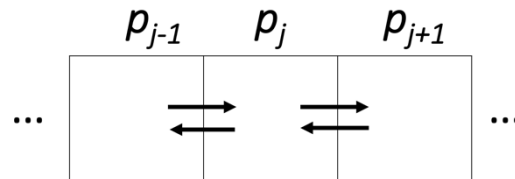
### 7.2.1.1. The relation of $k_{ex}$ to NetLogo's *diffuse*

The expression for  $k$ , the exchange rate (in units of  $s^{-1}$ ) is given by:

$$k = \frac{1}{n} \cdot \frac{f}{\Delta t}$$

Where  $f$  is the 2<sup>nd</sup> input parameter of the *diffuse* function that represents the fraction of  $Li$  in the patch that is being exchanged,  $n$  is the number of patch's neighbors ( $n=8$  in this system's topology), and  $\Delta t$  is the time step of the simulation.

### 7.2.1.2. The relation of the diffusion coefficient, $D$ , to NetLogo's *diffuse*



Let  $p$  be some measured property at spatial index  $j$  in a 1-dimensional grid, where  $\Delta x$  is the spatial interval and  $\Delta t$  is the time interval. Let  $n$  be the number of neighbors of each cell in the grid ( $n=2$  for this 1d example), and let  $f$  be the fraction of  $p$  that is being diffused away at each time step. The changes in the value of  $p_j$  with respect to a small change in time or space are denoted as  $\Delta_t p_j$  and  $\Delta_x p_j$ , respectively. After a single time-step,  $\Delta t$ , the change in the value of  $p_j$  is given by:

$$\begin{aligned} \Delta_t p_j &= \frac{f}{n} p_{j-1} - \frac{f}{n} p_j - \frac{f}{n} p_j + \frac{f}{n} p_{j+1} \\ &= \frac{f}{n} [(p_{j-1} - p_j) - (p_j - p_{j+1})] \\ &= \frac{f}{n} (\Delta_x (\Delta_x p_j)) \\ \frac{\Delta_t p_j}{\Delta t} &= \frac{\frac{f}{n} \Delta_x^2 p_j \Delta x^2}{\Delta t \Delta x^2} \\ \text{let } D &= \frac{f \Delta x^2}{n \Delta t} ; \text{ set } \Delta t \rightarrow 0, \Delta x \rightarrow 0 \\ \Rightarrow \frac{\partial p(x, t)}{\partial t} &= D \frac{\partial^2 p(x, t)}{\partial x^2} \end{aligned}$$



In NetLogo,  $f$  is the 2<sup>nd</sup> input parameter in “diffuse” function, and  $n=8$  (in this particular topology, corresponds with a 2d grid), so the relation between the diffusion equation and the model is straight forward:

$$D = \frac{f \Delta x^2}{8 \Delta t} \Rightarrow f = \frac{8 D \Delta t}{\Delta x^2}$$

The CFL (Courant–Friedrichs–Lewy) condition is expressed by the following limitation:

$$CFL \text{ condition: } 0 \leq f \leq 1$$

Reflecting that a single patch cannot diffuse to its neighbors more <sup>7</sup>Li than it has itself. For a given value of  $D$  (7.11E-15 m<sup>2</sup>/s, in this case), besides the CFL conditions, there are additional limitations when choosing the time and space steps: the spatial resolution of the model should be of a few microns (the NMR detection is only for the atoms in the skin depth range), but the time step should be computationally efficient, i.e., not too small.

### 7.2.2. Stability of the fitting parameters

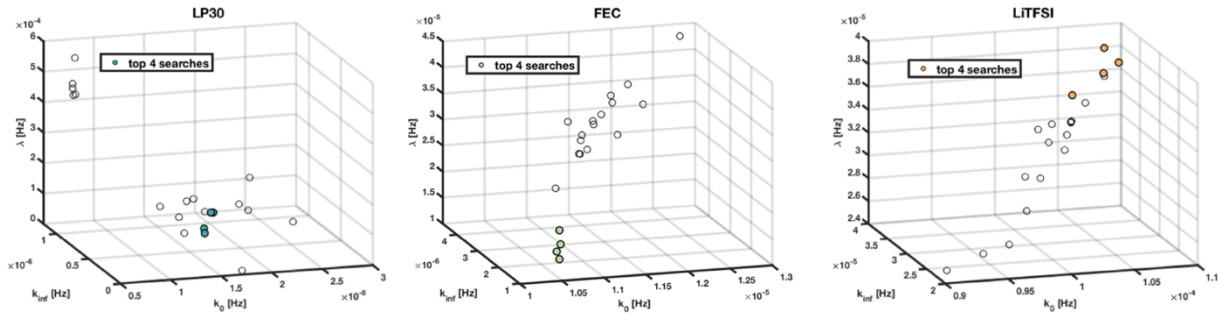


Figure S4: final results from 20 optimization searches for the three electrolytes (see titles of the subplots), visualized in a 3d parameter space.

Figure S4 shows the results (i.e., fitted values of  $\lambda$ ,  $k_0$ , and  $k_\infty$ ) from 20 independent searches, visualized on a 3d plot. The top four searches (i.e., the searches with the lowest MSE) for each experiment are

	LP30			FEC			LiTFSI		
	best fit	mean	std	best fit	mean	std	best fit	mean	std
<b>k<sub>0</sub> [Hz]</b>	<b>1.81E-06</b>	1.90E-06	1.23E-07	<b>1.06E-05</b>	1.06E-05	9.56E-08	<b>1.09E-04</b>	1.07E-04	1.91E-06
<b>k<sub>inf</sub> [Hz]</b>	<b>7.63E-07</b>	8.33E-07	1.25E-07	<b>1.43E-06</b>	1.37E-06	3.53E-07	<b>3.86E-05</b>	3.70E-05	1.48E-06
<b>corrosion constant [Hz]</b>	<b>2.43E-05</b>	3.32E-05	1.15E-05	<b>1.55E-05</b>	1.53E-05	1.15E-06	<b>3.83E-05</b>	3.69E-05	1.22E-06
<b>MSE</b>	<b>3.09E-04</b>	3.13E-04	4.69E-06	<b>7.22E-04</b>	7.23E-04	9.57E-07	<b>4.59E-04</b>	4.68E-04	1.02E-05

Table S1: fitting results including statistic regarding the top four searches

highlighted in colors. It can be clearly seen that the top results are closely grouped together, and this trend is observed in all three experiments. This indicates that the best optimization processes are converging to the same minima and that the solutions are unique. Table S1 shows the values of the fitted parameters with mean and standard deviation calculated from the top four searches.

### 7.2.3. Isotope exchange - Gunnarsdóttir et al.

Interestingly, the experimental results (i.e., the dynamics of LP30 and LP30/FEC) are somewhat different from ours. The exchange seems to be faster in the measurements done by Gunnarsdóttir et al. compared to the measurements in this research. Also, to fit their data, the input parameter  $SA\_factor$  had

	LP30			FEC			
	best fit	mean	std	best fit	mean	std	ratio FEC/LP30
$k_0$ [Hz]	<b>1.07E-05</b>	1.08E-05	1.49E-07	<b>1.94E-05</b>	1.92E-05	4.23E-07	1.8
$k_{inf}$ [Hz]	<b>2.86E-06</b>	2.89E-06	2.74E-08	<b>6.56E-06</b>	6.55E-06	4.35E-08	2.3
corrosion constant [Hz]	<b>2.02E-05</b>	2.10E-05	6.68E-07	<b>1.94E-05</b>	1.92E-05	9.01E-07	1
MSE	<b>3.10E-03</b>	3.20E-03	2.95E-05	<b>3.70E-03</b>	3.70E-03	6.08E-06	

Table S2: results from fitting the data from Gunnarsdóttir et al.; statistic values were calculated for the top three searches

to be fixed on a value that corresponds to  $SA \sim 20\%$  lower than the geometric surface area mentioned in their work. A possible explanation is that the pristine  ${}^6\text{Li}$  was initially covered with some passivation layer (not uniformly), which practically makes the *real* SA smaller than the geometric one. Smaller SA means more Li ions per Li metal at the surface, which makes sense since the amount of electrolyte used in their experiment was twice as high as what we used. The fitted values are summarized in Table S2, and the uniqueness of the solution is exemplified in Figure S5.

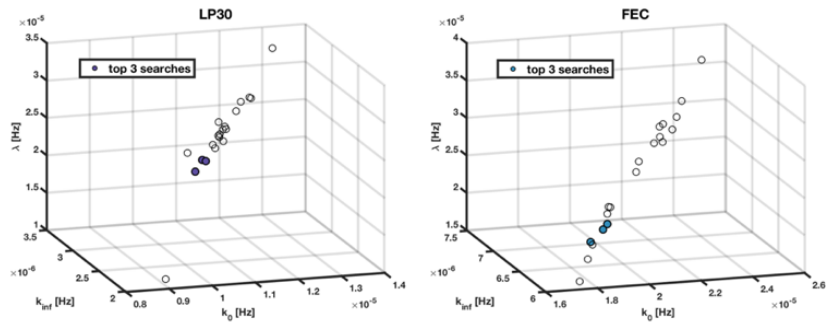


Figure S5: final results from 20 optimization searches. The best three searches are colored; the fact that all three searched are closely grouped indicates that the solution was converged.

#### 7.2.4. Sensitivity analysis to the skin effect

This analysis aims to determine the model's sensitivity to the NMR detection limitation and see if some approximations are justified.

##### 7.2.4.1. Sensitivity for different magnets

As can be seen from Eq. [10], the skin depth and the magnetic field are related such that:  $\delta \propto B_0^{-1/2}$ , meaning that the detection range is decreased at higher magnetic fields. Specifically, the skin depth determines how much Li is detected, so the expectation is that the same system would be

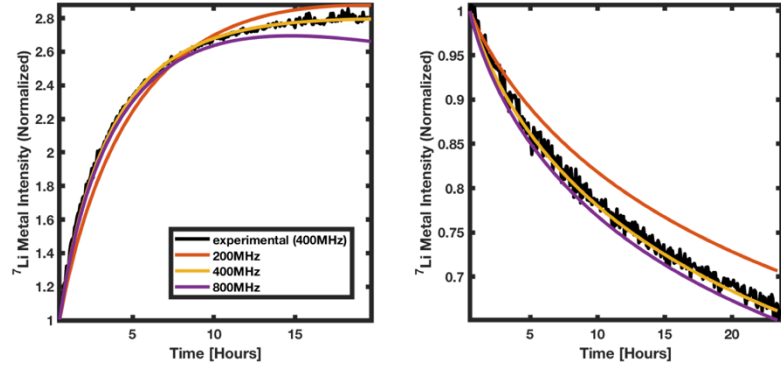


Figure S6: Simulation curves of metal exchange and self-diffusion (LiTFSI) for different values of skin depth. All other parameters were kept the same.

observed differently in different NMR magnets. Simulated curves of the metal intensity in different magnetic fields are plotted in Figure S6. According to the analysis, the model shows some sensitivity to the skin depth only where the difference in the magnetic fields is very large. Meaning, theoretically, performing the experiment in magnetic fields that are not significantly different (e.g., @400MHz and @300MHz) should yield pretty close results.

#### 7.2.4.2. Sensitivity to the method of numerical detection

In this analysis, it was checked whether implementation of an accurate NMR excitation across the skin depth of the metal is necessary or not. As shown in Figure S7, it is indeed significant: the red curve represents the simulation that was fitted to the experimental data (LiTFSI), implementing NMR detection that is based on theory (using  $\delta = 10.47\mu\text{m}$ ). The other simulated curves represent detection that was done approximately, i.e., summing all of the  $^7\text{Li}$  intensity in the first  $n$  metal patches. If the model was

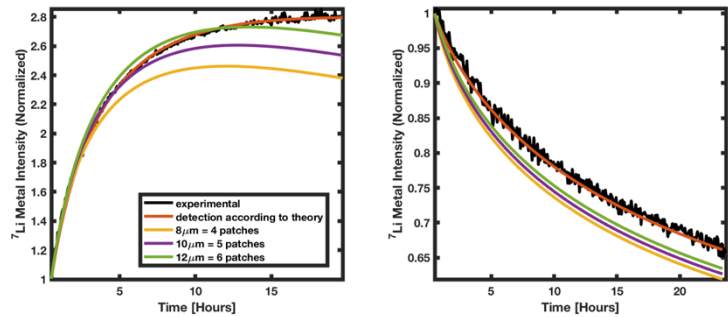


Figure S7: Simulation curves of metal exchange and self-diffusion (LiTFSI) for different values of skin depth, where the detection was approximated. All other parameters were kept the same.

not sensitive to detection method, we would expect the red and the purple curves, representing detection at a similar value of  $\delta$ , to be very close to another. However, as can be seen, the simulated curves are considerably different, indicating that the model is sensitive to numerical approximations.

### 7.2.5. Sensitivity to surface area

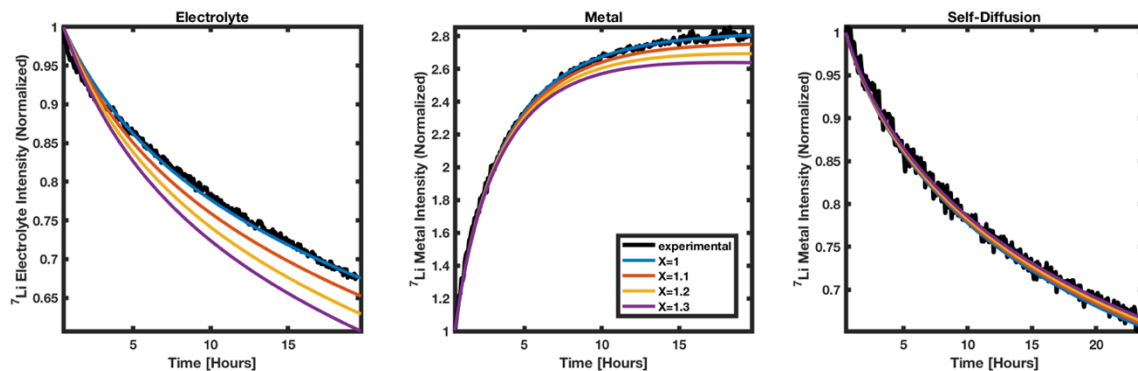


Figure S8: Simulation curves of metal exchange and self-diffusion ( $\text{LiTFSI}$ ) for different values of surface area. All other parameters were kept the same.

The sensitivity of the model to the surface area was checked for different values of  $X$  where  $X$  is defined as the deviation from the geometric surface area:

$$SA_{\text{geometric}} \leq SA \leq SA_{\text{geometric}} \cdot X$$

As can be seen in Figure S8 the simulated exchange curves (electrolyte and metal) are changed with  $X$ , implying that the model is sensitive to the value of the surface area.

### 7.2.6. Fitted $j_{\text{ex}}(t)$

Fitted values of  $j_{\text{ex}}(t)$  (using Eq. [6]) are plotted in Figure S9; absolute values of the exchange flux and the normalized values can be seen on the left and the right plots, respectively.

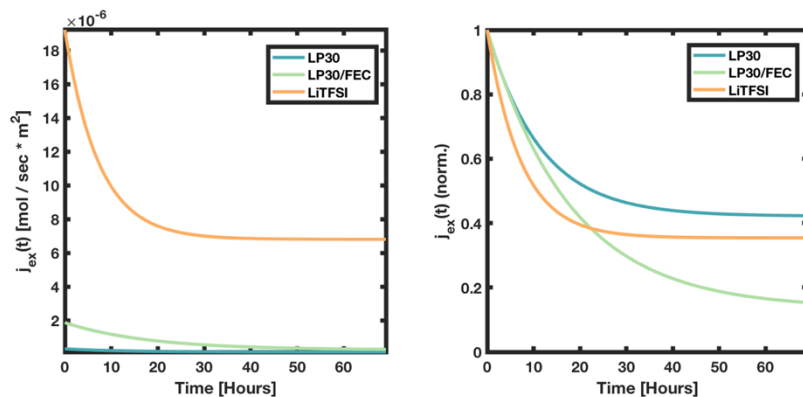


Figure S9: fitted  $j_{\text{ex}}(t)$  of the three systems, showing the absolute exchange flux as a function of time (left), and same curves normalized (right)

## 8. References

1. Goodenough, J. B. & Park, K. S. The Li-ion rechargeable battery: A perspective. *J. Am. Chem. Soc.* **135**, 1167–1176 (2013).
2. Gao, X. *et al.* Thermodynamic Understanding of Li-Dendrite Formation. *Joule* **4**, 1864–1879 (2020).

3. Bhattacharyya, R. *et al.* In situ NMR observation of the formation of metallic lithium microstructures in lithium batteries. *Nat. Mater.* **9**, 504–510 (2010).
4. Wood, K. N., Noked, M. & Dasgupta, N. P. Lithium metal anodes: Toward an improved understanding of coupled morphological, electrochemical, and mechanical behavior. *ACS Energy Lett.* **2**, 664–672 (2017).
5. Fang, C. *et al.* Quantifying inactive lithium in lithium metal batteries. *Nature* (2019) doi:10.1038/s41586-019-1481-z.
6. Gunnarsdóttir, A. B., Amanchukwu, C. V., Menkin, S. & Grey, C. P. Noninvasive In Situ NMR Study of “Dead Lithium” Formation and Lithium Corrosion in Full-Cell Lithium Metal Batteries. *J. Am. Chem. Soc.* (2020) doi:10.1021/jacs.0c10258.
7. Peled, E. The Electrochemical Behavior of Alkali and Alkaline Earth Metals in Nonaqueous Battery Systems—The Solid Electrolyte Interphase Model. *J. Electrochem. Soc.* **126**, 2047–2051 (1979).
8. Gauthier, M. *et al.* Electrode-Electrolyte Interface in Li-Ion Batteries: Current Understanding and New Insights. *J. Phys. Chem. Lett.* **6**, 4653–4672 (2015).
9. He, X. *et al.* The passivity of lithium electrodes in liquid electrolytes for secondary batteries. *Nat. Rev. Mater.* **6**, 1036–1052 (2021).
10. Winter, M. The solid electrolyte interphase - The most important and the least understood solid electrolyte in rechargeable Li batteries. *Zeitschrift für Phys. Chemie* **223**, 1395–1406 (2009).
11. Wang, Z. *et al.* An Anion-Tuned Solid Electrolyte Interphase with Fast Ion Transfer Kinetics for Stable Lithium Anodes. *Adv. Energy Mater.* **10**, 1–9 (2020).
12. Jorn, R., Raguette, L. & Peart, S. Investigating the Mechanism of Lithium Transport at Solid Electrolyte Interphases. *J. Phys. Chem. C* **124**, 16261–16270 (2020).
13. Guo, R., Wang, D., Zuin, L. & Gallant, B. M. Reactivity and Evolution of Ionic Phases in the Lithium Solid-Electrolyte Interphase. *ACS Energy Lett.* **6**, 877–885 (2021).
14. Küpers, V., Kolek, M., Bieker, P., Winter, M. & Brunklaus, G. In situ <sup>7</sup>Li-NMR analysis of lithium metal surface deposits with varying electrolyte compositions and concentrations. *Phys. Chem. Chem. Phys.* **21**, 26084–26094 (2019).
15. Haber, S. & Leskes, M. What Can We Learn from Solid State NMR on the Electrode–Electrolyte Interface? *Adv. Mater.* **30**, (2018).
16. Ilott, A. J. & Jerschow, A. Probing Solid-Electrolyte Interphase (SEI) Growth and Ion Permeability at Undriven Electrolyte-Metal Interfaces Using <sup>7</sup>Li NMR. *J. Phys. Chem. C* **122**, 12598–12604 (2018).
17. Gunnarsdóttir, A. B., Vema, S., Menkin, S., Marbella, L. E. & Grey, C. P. Investigating the effect of a fluoroethylene carbonate additive on lithium deposition and the solid electrolyte interphase in lithium metal batteries using: In situ NMR spectroscopy. *J. Mater. Chem. A* **8**, 14975–14992 (2020).

18. Le Mehaute, A. & Crepy, G. Introduction to transfer and motion in fractal media: The geometry of kinetics. *Solid State Ionics* **9–10**, 17–30 (1983).
19. Turon Teixidor, G., Park, B. Y., Mukherjee, P. P., Kang, Q. & Madou, M. J. Modeling fractal electrodes for Li-ion batteries. *Electrochim. Acta* **54**, 5928–5936 (2009).
20. Van Zijl, P. C. M. & Yadav, N. N. Chemical exchange saturation transfer (CEST): What is in a name and what isn't? *Magn. Reson. Med.* **65**, 927–948 (2011).
21. Zaiss, M. & Bachert, P. Chemical exchange saturation transfer (CEST) and MR Z-spectroscopy in vivo: A review of theoretical approaches and methods. *Phys. Med. Biol.* **58**, (2013).
22. Zaiss, M. *et al.* QUESP and QUEST revisited – fast and accurate quantitative CEST experiments. *Magn. Reson. Med.* **79**, 1708–1721 (2018).
23. Zaiss, M., Schnurr, M. & Bachert, P. Analytical solution for the depolarization of hyperpolarized nuclei by chemical exchange saturation transfer between free and encapsulated xenon (HyperCEST). *J. Chem. Phys.* **136**, 144106 (2012).
24. Zaiss, M. & Bachert, P. Exchange-dependent relaxation in the rotating frame for slow and intermediate exchange - modeling off-resonant spin-lock and chemical exchange saturation transfer. *NMR Biomed.* **26**, 507–518 (2013).
25. Kozen, A. C. *et al.* Stabilization of Lithium Metal Anodes by Hybrid Artificial Solid Electrolyte Interphase. *Chem. Mater.* (2017) doi:10.1021/acs.chemmater.7b01496.
26. Wang, A., Kadam, S., Li, H., Shi, S. & Qi, Y. Review on modeling of the anode solid electrolyte interphase (SEI) for lithium-ion batteries. *npj Comput. Mater.* **4**, (2018).
27. Zhai, P. *et al.* In Situ Generation of Artificial Solid-Electrolyte Interphases on 3D Conducting Scaffolds for High-Performance Lithium-Metal Anodes. *Adv. Energy Mater.* (2020) doi:10.1002/aenm.201903339.
28. Tan, J., Matz, J., Dong, P., Shen, J. & Ye, M. A Growing Appreciation for the Role of LiF in the Solid Electrolyte Interphase. *Adv. Energy Mater.* **2100046**, 1–25 (2021).
29. Feher, G. & Kip, A. F. Electron spin resonance absorption in metals. I. Experimental. *Phys. Rev.* **98**, 337–348 (1955).
30. Dyson, F. J. Electron Spin Resonance Absorption in Metals. II. Theory of Electron Diffusion and the Skin Effect. *Phys. Rev.* **98**, 349–359 (1955).
31. Ilott, A. J. & Jerschow, A. Super-resolution Surface Microscopy of Conductors using Magnetic Resonance. *Sci. Rep.* **7**, 1–7 (2017).
32. Guo, R. & Gallant, B. M. Li<sub>2</sub>O Solid Electrolyte Interphase: Probing Transport Properties at the Chemical Potential of Lithium. *Chem. Mater.* **32**, 5525–5533 (2020).
33. He, M., Guo, R., Hobold, G. M., Gao, H. & Gallant, B. M. The intrinsic behavior of lithium fluoride in solid electrolyte interphases on lithium. *Proc. Natl. Acad. Sci. U. S. A.* **117**, 73–79 (2020).
34. Van Dyke Parunak, H., Savit, R. & Riolo, R. L. Agent-Based Modeling vs. Equation-Based

- Modeling: A Case Study and Users' Guide. 10–25 (1998) doi:10.1007/10692956\_2.
35. Wilensky, U. & Rand, W. *An introduction to agent-based modeling: modeling natural, social, and engineered complex systems with NetLogo*. (Mit Press, 2015).
  36. Wilensky, U. NetLogo. (1999).
  37. Stonedahl, F., & Wilensky, U. BehaviorSearch. (2010).
  38. Guo, Y. *et al.* An Autotransferable g-C<sub>3</sub>N<sub>4</sub> Li<sup>+</sup>-Modulating Layer toward Stable Lithium Anodes. *Adv. Mater.* **31**, 1–10 (2019).
  39. Fairhurst, D., Cosgrove, T. & Prescott, S. W. Relaxation NMR as a tool to study the dispersion and formulation behavior of nanostructured carbon materials. *Magn. Reson. Chem.* **54**, 521–526 (2016).
  40. Weber, R. *et al.* Surface Area of Lithium-Metal Electrodes Measured by Argon Adsorption. *J. Electrochem. Soc.* **166**, A3250–A3253 (2019).

## 9. Acknowledgments

First and foremost, I want to thank my *awesome* thesis advisor, Dr. Michal Leskes, who helped me grow and become a scientist during the last two years. With her unique attitude, she provided me the guidance and the tools I needed yet gave me the freedom and the confidence to follow my ideas and walk in my own way. It was an absolute pleasure to work with her and learn from her.

I want to thank each of my current and former group members for being an essential part of my journey: Dr. Vaishali Arunachalam, Dr. Brijith Thomas, Dr. Daniel Jardon-Alvarez, Dr. Ilia Moroz, Dr. Arava Zohar, Shira Haber, Asya Svirinovsky, Dr. Ran-Eitan Abutbul, Yuval Steinberg, Shakked Schwartz, Dr. Ayan Maity, Chen Oppenhime, Tom Granot, and Yuri Shakhman.

I want to thank Dr. Liat Avram-Biton for her technical help in the NMR measurements and for her valuable insights.

Finally, I would like to express my gratitude and appreciation to my partner in life, Inbal, for her never-ending support, listening, and advice along the way.